Anatomy of thermal unrest at a hydrothermal system: case study of the 2021–2022 crisis at Vulcano

Sophie Pailot-Bonnétat, Victoria Rafflin, Andrew Harris, Iole Serena Diliberto, Gaetana Ganci, Guiseppe Bilotta, Annalisa Cappello, Guillaume Boudoire, Fausto Grassa, Alessandro Gattuso, et al.

Pailot-Bonnétat *et al.*
Earth, Planets and Space (2023) 75:159
https://doi.org/10.1186/s40623-023-01913-5

Earth, Planets and Space

FRONTIER LETTER

Open Access

Anatomy of thermal unrest at a hydrothermal system: case study of the 2021–2022 crisis at Vulcano

Sophie Pailot-Bonnétat[1*], Victoria Rafflin[1], Andrew Harris[1], Iole Serena Diliberto[2], Gaetana Ganci[2], Guiseppe Bilotta[2], Annalisa Cappello[2], Guillaume Boudoire[1], Fausto Grassa[2], Alessandro Gattuso[2] and Michael Ramsey[3]

Abstract

Hydrothermal systems can generate phreatic and/or phreatomagmatic explosions with little warning. Understanding the temporal and spatial evolution of geophysical and geochemical signals at hydrothermal systems is crucial for detecting precursory signs to unrest and to inform on hazard. Thermal signatures of such systems are poorly defined because data records are often too short or discrete compared to activity timescales, which can be decadal. La Fossa system of Vulcano has been monitored since the 1980s and entered a period of unrest in 2021. We assessed the thermal signature of La Fossa using ground- and satellite-based data with various temporal and spatial scales. While continuously-recording stations provided continuous but point-based measurements, fumarole field vent surveys and infrared images obtained from satellite-flown sensors (ASTER and VIIRS) allowed lower temporal resolution but synoptic records to be built. By integrating this multi-resolution data set, precursory signs of unrest could retrospectively be detected from February to June 2021. Intensity of all unrest metrics increased during summer 2021, with an onset over a few days in September 2021. By September, seismic, CO_2, SO_2 and other geochemical metrics also indicated unrest, leading Civil Protection to raise the alert level to yellow on October 1. Heat flux, having been 4 MW in May 2019, increasing to 90 MW by September, and peaking at 120 MW in March 2022. We convolved our thermal data sets with all other monitoring data to validate a Vulcano Fossa Unrest Index (VFUI), framework of which can be potentially applied to any hydrothermal system. The VFUI highlighted four stages of unrest, none of which were clear in any single data set: background, precursory, onset and unrest. Onset was characterized by sudden release of fluids, likely caused by failure of sealed zones that had become pressurized during the precursory phase that began possibly as early as February 2021. Unrest has been ongoing for more than 18 months, and may continue for several more years. Our understanding of this system behavior has been due to hindsight, but demonstrates how multiparametric surveys can track and forecast unrest.

Keywords Hydrothermal system, Heat flux, Vulcano, Unrest, Satellite remote sensing

*Correspondence:
Sophie Pailot-Bonnétat
sophie.pailot_bonnetat@uca.fr
Full list of author information is available at the end of the article

Graphical Abstract

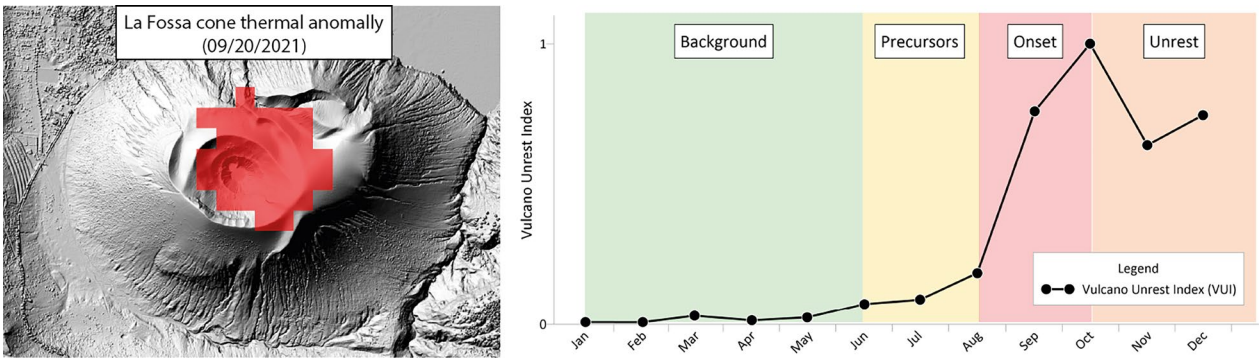

Introduction

Unrest at hydrothermal systems involves changes in the gas composition and flux, heightened heat flux, seismicity and/or deformation (e.g., Capasso et al. 1997; De Natale et al. 1999; Orsi et al. 1999; Sachpazi et al. 2002; Gottsmann et al. 2007; Werner et al. 2008; Gambino and Guglielmino 2008; Alparone et al. 2010; Christenson et al. 2010). Defining and tracking unrest at hydrothermal systems is fundamental for hazard assessment, as well as for understanding system dynamics and the association with explosive activity (Montanaro et al. 2022). Hydrothermal systems associated with non-eruptive, fumarolic degassing are liable to generate phreatic eruptions with little warning (e.g., Kato et al. 2015; Hamling 2017; Mayer et al. 2017), as well as phreatomagmatic eruptions which may have longer precursory periods (e.g., Chouet and Matoza 2013; Geshi et al. 2016; Ardid et al. 2022).

Whether unrest leads to explosive activity or not, geophysical signals recorded for restless systems can provide insights into physical and dynamic processes in operation, in and above the hydrothermal system (Montalto 1994; Mannen et al. 2018; Moretti et al. 2020; Girona et al. 2021). In addition, even unrest that does not lead to explosive activity presents hazards as sometimes testified by high contents of toxic gases in the ambient air, as for example at Mammoth Mountain (USA) during 1989 (Sorey et al. 2000).

However, some metrics or signs of unrest are poorly defined, and this includes the thermal signature. This is mostly because temperature measurements tend to be punctual and so define the thermal character of the system only for a particular point in a cycle of unrest, and lack the temporal resolution and duration to capture a complete cycle (Aubert 1999; Matsushima et al. 2003). As a result, continuous, high-temporal resolution thermal data sets recording the onset of unrest are lacking.

The ground temperature for points within the fumarole field of Vulcano's La Fossa system (Aeolian Islands, Italy) have been monitored since 1984 (Diliberto 2011). In addition, surveys have been repeated annually since 1995 to detect changes of vent temperatures across the field (Harris and Maciejewski 2000; Harris et al. 2012), and ASTER and Landsat Thematic Mapper imagery have been used to constrain the thermal anomaly associated with the fumarolic activity and derive heat flux (Gaonac'h et al. 1994; Harris and Stevenson 1997; Silvestri et al. 2019; Mannini et al. 2019). Since January 2020 onwards, we have also been running up to five continuously recording temperature sensor stations in and around the fumarole field. In parallel, we have completed fumarole temperature up to three times a year, coupled with infrared camera imaging. Over the summer of 2021 Vulcano's hydrothermal system entered a new phase of unrest, which allowed us to record and define the thermal signature of unrest. The northern hemisphere, Mediterranean summer generally runs from June through August, and the winter from December through February; where the summer solstice in 2021 was on 21 June, and the winter solstice was on 21 December.

We thus use the unrest that began in the second half of 2021 to define its signature in different thermal data sets, and examine how the temperature trends couple with other geochemical and geophysical data sets. This allows us to develop a model whereby unrest is preceeded by three-to-four months of slowly increasing heat flux, before an abrupt increase at the onset of unrest, with heat flux increasing by 10 s of MW over just one or two days.

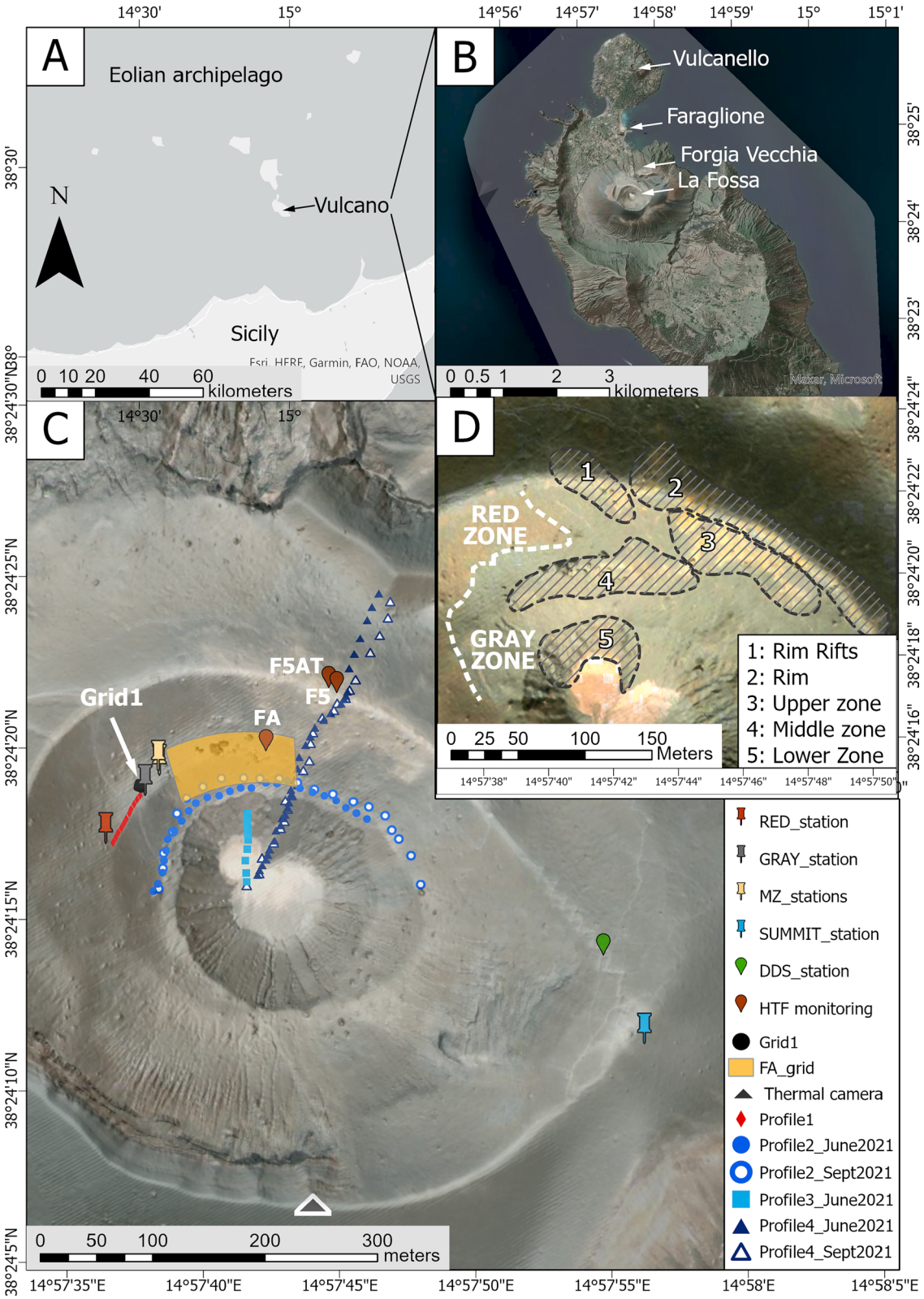

Fig. 1 **A** Location of Vulcano island in the Eolian Archipelago, Sicily. **B** Areas of interest in Vulcano island. **C** Location of permanent stations and punctual measurements. **D** Location of the limit between hot (GRAY) and cold (RED) zones, and the five zones of intense fumaroles release. *HTF* High Temperature Fumarole being F5AT, F5 and FA

Geological setting and context

Vulcano is located in the southern part of the Eolian Archipelago (Fig. 1A) and is the emerged summit of a volcanic edifice that extends c. 1000 m b.s.l. (below sea level) (De Astis et al. 2013). It is a composite volcanic system built during a series of eruptive phases, with first activity being dated at 130 ka (Keller 1980; De Astis et al. 2013). Structures and vents are aligned NNW-SSE, an alignment which is controlled by the Tindari-Letojanni strike-slip fault system that passes beneath the island (Ventura 1994; Mazzuoli et al. 1995; De Astis et al. 2013). The associated NE-SW extensional stress field is linked to the two major calderas on the island, the Piano and the Fossa, which have been interpreted as pull-apart basins (Ventura 1994; Mazzuoli et al. 1995), as well as the alignment of zones of fumarolic activity.

Thermal signature associated with fluid ascent at the Vulcano hydrothermal system

The Fossa, Faraglione and Vulcanello eruptive centers (Fig. 1B) have been active since 5.5 ka (De Astis et al. 2013). The last eruption occurred in AD 1888–1890, and its description by Mercalli and Silvestri (1891) became the archetype for Vulcanian eruptions (Mercalli 1907). Mercalli (1883) noted that emissions during late 1879 were sufficiently high that access to the crater for mining became impossible. De Fiore (1922) noted the establishment of a new fumarole field (maximum temperature 110 °C) in the Fossa crater by 1913, and Sicardi (1940) recorded increasing then decreasing temperatures between 1923 and 1937. The maximum recorded was 615 °C in 1924 (De Fiore 1924).

Fumarolic activity is mainly located in La Fossa crater and on the Spiaggia di Levante beach (Tedesco et al. 1995). While Ferrucci et al. (1991) found a magma body at 2–3 km depth, the magmatic contribution to the fumarolic gases has been inferred from chemical composition, helium isotope ratios and 3He output (Nuccio et al. 1999). Many authors have interpretated the gas composition at Vulcano as resulting from mixing of magmatic and deep hydrothermal fluids (marine and meteorological sources), with the hydrothermal system being a biphase (water–vapor) boiling saline solution (e.g., Carapezza et al. 1981; Chiodini and Cioni 1995; Nuccio et al. 1999). Carapezza et al. (1981) calculated that this saline solution was boiling at a temperature of 330–340 °C at a pressure of 13–17 MPa; Nuccio et al. (1999) assumed these P–T conditions in late 1970's, whereas P–T values around 400 °C and 20 MPa were hypothesized during the 1990s.

Mixing models have shown that unrest is associated with increased CO_2 and He fluxes, representing gas liberated by vesiculated magma (Nuccio et al. 1999). Background values of these gases are interpreted as being derived mainly from diffuse degassing of volatile impoverished melt (Nuccio et al. 1999). The unrest of 1988–96 was characterized by homogenization of the mixing fractions. This effect was interpreted as vaporization due to boiling, transforming the system from biphase to vapor-monophase; able to supply a uniform composition to all fumaroles (Nuccio et al. 1999). Fumarole temperatures also reached a maximum of 690 °C (Capasso et al. 1994; Chiodini and Cioni 1995), the area of fumarolic emission increased (Bukumirovic et al. 1997; Italiano et al. 1998), and the isotopic signature evolved toward a clear magmatic component (Tedesco et al. 1991; Capasso et al. 1997).

Since the late 1990s, fumarole temperatures have generally decreased (Diliberto 2011, 2017; Harris et al. 2012), and the biphase system has re-established. Gas expansion during ascent, and the subsequent gas temperature on emission is, however, highly dependent on rock permeability over the last few hundred meters (Nuccio et al. 1999). Changes in shallow permeability can trigger heating phases (increases in fumarole temperature), where increases in permeability associated with fracturing of sealed zones allow more efficient heat flux without new magmatic input (Diliberto 2011, 2017; Harris et al. 2012). Increased permeability has also been shown to relate to deflation, of a source at sea level, due to enhanced steam emission and a consequent reduction in volume of water in the hydrothermal system (Gambino and Guglielmino 2008; Harris et al. 2012).

The new (2021–present) phase of unrest

After around two decades of declining levels of thermal activity (Harris et al. 2012; Mannini et al. 2019), a new period of unrest was registered during the summer of 2021. CO_2, SO_2 fluxes and temperature data from the INGV monitoring network revealed slowly increasing emissions starting in June 2021, with a sharp increase in September 2021 (Inguaggiato et al. 2022a). The number of Very Long Period (VLP) seismic events also increased in September 2021, and was accompanied by 2 cm of inflation, indicating fluid pressurization within fractures (Federico et al. 2023). The temperature of the fumaroles increased, but the maximum temperature (372 °C) remained around the critical temperature of the Fossa crater boiling saline solution (~400 °C) and was very localized (Federico et al. 2023). This meant that, in contrast to the 1988–96 unrest, the hydrothermal system underwent only partial vaporization, so the system did not completely dry out and the biphase state was maintained (Federico et al. 2023).

Re-mobilization of sulfur stored in the system was also observed in direct measurements of SO_2 flux and

plume chemistry (Aiuppa et al. 2022). It also resulted in the eruption and deposition of sulfur (Additional file 1: Appendix A). Sulfur melting and emission of molten sulfur is not rare during unrest at Vulcano, where sulfur flow activity was common during the 1988–96 unrest (Harris et al. 2000, 2004). Sulfur melts between 112 and 120 °C (Meyer 1976), so heating of sulfur deposits in the shallow system above this temperature range during unrest will cause them to fluidize and erupt. However, between 1998 and 2020, no new eruptive sulfur structures, such as the hornitos, flows or air fall were observed, and the degree of sulfur deposition was markedly reduced.

Thermal character of the fumarole field

Heat flux at a fumarole field is partitioned between diffuse soil emissions and emission at fumarole vents (Sekioka and Yuhara 1974; Chiodini et al. 2005; Harris 2013). Unlike at some systems, e.g., La Soufriere (Jessop et al. 2021), the heat flux at Vulcano has been proven to be dominated by the diffuse component, as shown by independent studies based on the water flux, satellite remote sensing, thermal camera, and fumarole temperature measurements (Chiodini et al. 2005; Harris et al. 2009; Mannini et al. 2019). This is also the case at Nisyros (Greece) and Campi Flegrei's Solfatara (Chiodini et al. 2005). At such systems, the source of the heat has been ascribed to condensation of ascending fluids (Chiodini et al. 2005), where heat is then transferred to the surface by permeable convection and, over the last meter, conduction (Aubert 1999). Heat is then lost from the surface by radiation and convection (Sekioka and Yuhara 1974; Harris 2013).

At Vulcano, the zone of fumaroles is thus surrounded within a broader zone of soil emission. Heat flux from the zone of soil emission dominates the energy budget, accounting for 93 ± 2% of the total budget, where total heat fluxes were in the range 5–13 MW between 2000 and 2019. Reducing conditions within the soil emission zone changed the surface color from red to gray (Fig. 1D). We here label the former zone hot (grey) zone, and the latter cold (red). However, although accounting for less than 8% of the total flux, changes in the thermal character (number and temperature) of the fumaroles provides information on whether the system is heating or cooling (Harris and Maciejewski 2000; Matsushima et al. 2003), as well as on localized changes in shallow system permeability (Harris et al. 2012).

Methods

Between January 2020 and January 2022, we carried out six field campaigns, spaced by three to eight months. We carried out thermal measurements in January and October 2020, March, June and September 2021, and January 2022. This sampling frequency was limited by travel restrictions and lockdowns due to the Covid pandemic. The full list of measurements and their locations as well as instruments used is given in Additional file 1: Appendix B.

Surface temperature measurements

Two temperature stations separated by 50 m were installed in January 2020 at the west edge of the fumarole field: RED_station and GRAY_station (Fig. 1C). Each station records temperature at 15 cm depth (T_{15}), surface temperature and air temperature 5 cm above ground level, every 5 or 10 min. Two other temperature stations (MZ1 and MZ2) were installed inside the hot zone at the end of June 2021 (Fig. 1C). In addition, we used data from the permanent station maintained by INGV-PA (DDS station, Fig. 1C) on the east side of the fumarole field and HTF (high temperature fumarole) FA, F5 and F5AT (Fig. 1C). DDS station provides temperature at 15, 30, 45 and 60 cm depths. During each campaign, T_{15} and surface temperature were measured every 5 m along a 50 m-long profile (Profile1, Fig. 1C) between RED_station and GRAY_station (Fig. 1D), every 1 m within a 5×5 m grid (Grid1, Fig. 1C), and every 15 m on 250 m and 300 m long profiles traversing the entire field (Profiles 2, 3 and 4, Fig. 1C). In March and June 2021, we also made T_{15} measurements for every 5 m across a 110×50 m grid (FA_grid, Fig. 1C). Once the 2021 unrest began, we could not resume the FA_grid measurements due to dangerous conditions. However, simultaneous measurements at Grid1 in March and June allowed us to assess the representativeness of the 5×5 m area. Detailed descriptions of the temperature measurements at FA_grid are given in Additional file 1: Appendix B.

Soil CO_2 flux measurements

Soil CO_2 flux (g m^{-2} d^{-1}) was measured using the accumulation chamber method of Chiodini et al. (1998). Data was processed with the "Flux Revision" software (https://www.westsystems.com/download/) using the raw soil CO_2 content regression line measured by the instrument and ambient pressure–temperature (acquired from a Kestrel 5500 hand held weather station) to obtain the flux (ppm s^{-1}). Conversion in (g m^{-2} d^{-1}) is obtained by considering the volume and area of the chamber together with air temperature and pressure.

Fumarole surveys

Once a year since 1994, and two to three times a year since 2020, a survey using Thermal InfraRed (TIR) thermometers was conducted to measure vent temperatures. The survey was always conducted following the same

path and pattern to assure its statistical consistency. On the basis of historical evolution and thermal characteristics, the fumarole field was divided into five zones by Harris and Maciejewski (2000). These are: (1) the rim rifts which are two fissures that cut across the rim on the west edge of the field, (2) fumaroles in fractures aligned along the rim, the (3) upper, (4) middle and (5) lower zones (Fig. 1D).

Thermal images

Night time thermal images were acquired coincident with scheduled satellite overpasses (Ramsey 2016). The camera was placed opposite the fumarole field, on south rim of the crater (Fig. 1C). This position allows a synoptic view of the five fumarole zones from the rim to the bottom of the crater. For a line-of-sight distance of 310 m to the bottom of the crater and 460 m to the rim, the pixel size ranged from 0.4 m to 0.6 m. To image the entire field, a panel of three images was taken as a panorama.

ASTER processing

ASTER (Advanced Spaceborne Thermal Emission and Reflection Radiometer) is a sensor flown on the TERRA NASA's low earth orbit satellite, which measures spectral radiance at 14 wavebands between the visible and thermal infrared. Given that we are interested in kinetic surface temperature, we here use data from the five Thermal Infrared (TIR) bands between 8 and 12 μm. Specifically, we used the AST_08 image product with 90-m pixel resolution, in which pixel temperatures are automatically corrected for emissivity and atmospheric effects. Nighttime scenes were selected to avoid solar heating and thermal inertia effects. Masking allowed extraction of temperature data for each pixel in two regions of interest (ROI): the Fossa crater, where the anomaly is visible, and Vulcanello, a cone north of the Fossa which currently has no anomalous heat and gas release (Fig. 1B). Maximum and mean temperatures from the ambient control (Vulcanello) were compared to those of the active target (i.e., the Fossa).

Within the Fossa ROI, the number of anomalous pixels was calculated using the temperature distribution (Additional file 1: Appendix D). Almost all distributions are bimodal: the first mode being the background temperature distribution and the second the anomaly (Fig. 2a). If heating occurs, the hot part of the distribution becomes more robust making it more skewed to hot temperatures. Pixel location in terms of ground target and viewing angles are variable from overpass to overpass, which might affect the clarity of the bimodality. However, the pixels detected in this study are coherent with thermal anomaly location and evolution found in situ. The number of pixels within the second mode was extracted and multiplied by the pixel area to obtain the thermal anomaly area (Fig. 2b; Additional file 1: Appendix D). This method was validated by cross-comparison with an independent deep learning approach (supervised UNET network) (Corradino et al. 2023).

Conversion to heat flux

Following Sekioka and Yuhara (1974) and Matsushima et al. (2003), radiative (*Mrad*) and convective (*Mconv*) heat fluxes were calculated on pixel-by-pixel basis in ASTER and thermal camera images, as follows:

$$M_{rad} = \sigma \varepsilon \left(T_a^4 - T_b^4 \right), \tag{1}$$

$$M_{conv} = h_c (T_a - T_b), \tag{2}$$

where σ is the Stefan-Boltzmann constant, ε is emissivity, h_c is the convective heat transfer coefficient, T_a is the temperature of the anomalous pixel, and T_b is background temperature. Multiplying by pixel area converts these values from flux densities (M in W m^{-2}) to heat fluxes (Φ in J s^{-1}). For emissivity, we used the mean of our measured values (see Additional file 1: Appendix B) and for h_c, we used 24 J K^{-1} after Sekioka and Yuhara (1974) and Matsushima et al. (2003). For the background temperatures, we used the minimum and mean temperatures of non-anomalous pixels. Values were summed for all pixels to obtain total Φrad and Φconv and the totals were added to obtain total heat flux [Φtot = Φrad + Φconv].

VIIRS processing

VIIRS (Visible Infrared Imaging Radiometer) is a sensor flown on the NASA/NOAA Suomi National Polar-orbiting Partnership and NOAA-20 low earth orbit satellites. VIIRS measures spectral radiance at 22 wavebands between the visible and thermal infrared, where we used data from two of the mid-infrared band I4 (3.55–3.93 μm) and the TIR band I5 (10.5–12.4 μm) which have pixel sizes of 375 m.

VIIRS data were analyzed using a specialized version of CL-HOTSAT (Ganci et al. 2016). CL-HOTSAT is a satellite data processing system used both for the near-real-time monitoring of high-temperature volcanic features (Rogic et al. 2019; Ganci et al. 2023) and for the extraction of the input parameters of numerical models used for lava flow hazard and risk assessment (Cappello et al. 2016; Zuccarello et al. 2022). The VIIRS data were downloaded as Level 1 Sensor Data Record (SDR) format including L1B calibrated radiance products VNP02IMG and VJ102IMG, for SNPP and JPSS-1/NOAA20 platforms respectively, and VNP03IMG and VJ103IMG VIIRS L1 terrain-corrected geolocation products

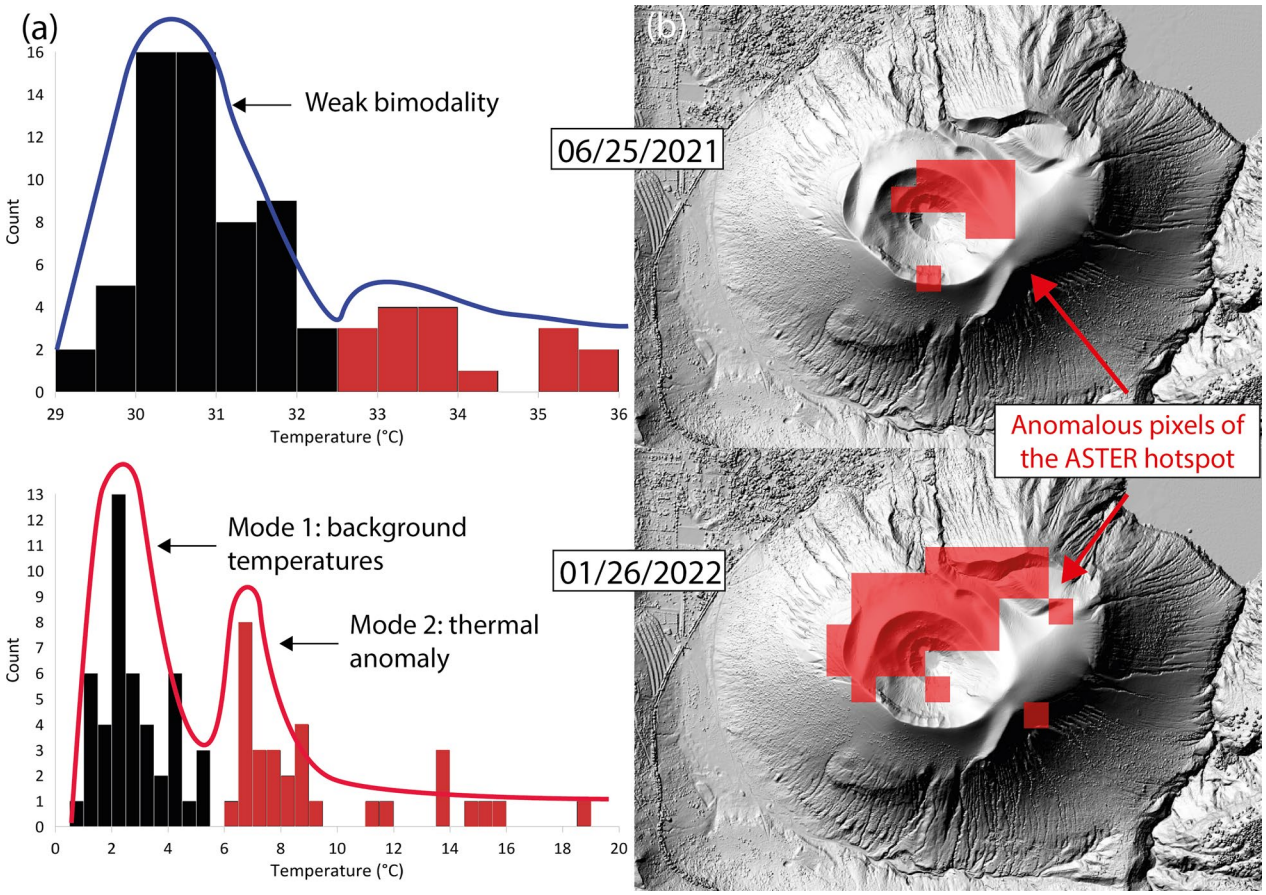

Fig. 2 **a** Examples of surface temperature frequency distribution on ASTER images. The distribution starts weakly bimodal with a positive tail and the bimodality increases along with the thermal anomaly. Mode 1 is interpreted as the background reference temperature and mode 2 as the anomalous temperature in the ROI area. **b** Examples of anomalous pixel locations selected following the temperature frequency distribution

containing the derived line-of-sight (LOS) vectors for each of the 375-m image-resolution or I-bands. The geolocation product was used for reprojecting and georeferencing the calibrated radiances that were then corrected for the atmospheric effect. Nighttime images were selected to avoid possible effects due to solar reflection. Moreover, in order to locate the thermally anomalous pixels a new hotspot detection algorithm was developed based on the Normalized Thermal Index (NTI) computed using the I4 and I5 bands (Wright et al. 2002).

$$NTI = \frac{I4 - I5}{I4 + I5}. \tag{3}$$

This hotspot algorithm is a contextual algorithm in CL-HOTSAT where the volcanic area includes the whole La Fossa crater area and the non-volcanic area the rest of the island. We flag a pixel in the volcanic area as a hotspot if its value for NTI (NTIHS) is greater than the normal variation of NTI in a non-volcanic area (NTINVA) according to:

$$NTIHS > Mean_{NTINVA} + 3 * SD_{NTINVA}. \tag{4}$$

For each pixel flagged as a hotspot the radiant heat flux is computed by assuming the pixel as composed by two thermal components. A dual band technique is then applied to the hotspot pixel in order to infer their thermal structures and the Stefan-Boltzmann law is applied to compute the associated radiant heat flux.

Results

Punctual measurements of temperature and soil CO_2 flux

Since 2020, the location of the transition between the cold and hot zones on Profile1 has been stable and located at the 20 m mark (Fig. 3). Between September 2015 and March 2021, T_{15} for the cold zone was stable, the temperature range for any given measurement time varying by no more than 3 °C (Additional file 1: Appendix

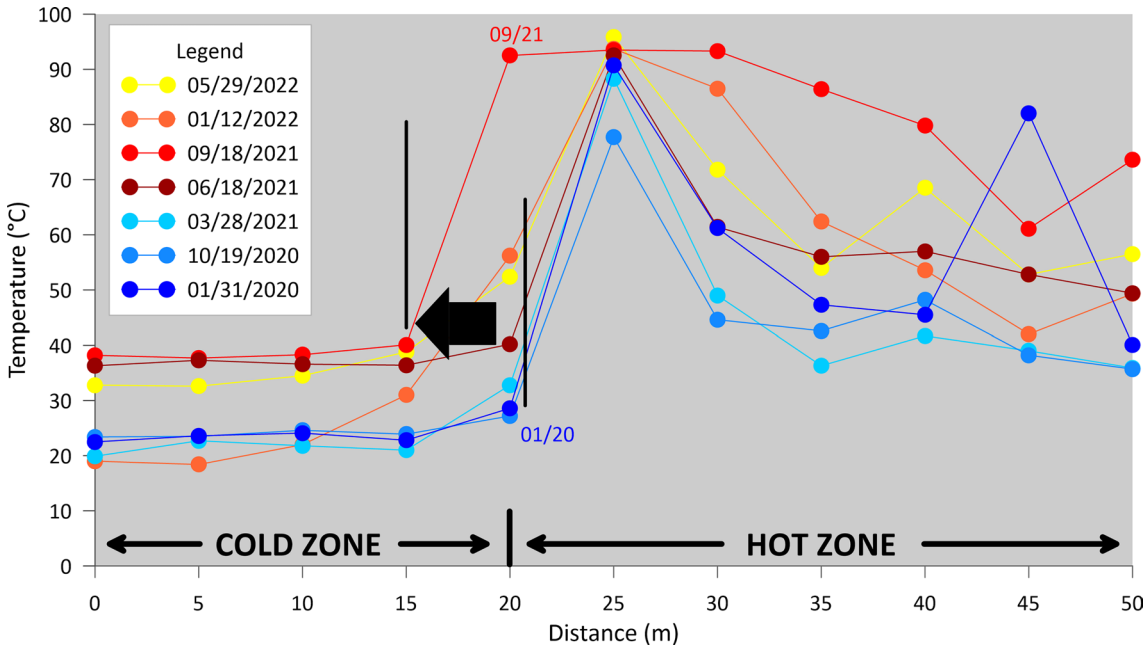

Fig. 3 Temperature at 15 cm depth on Profile1 west of the fumarole field (2019–2022) (see Fig. 1C for location). The large black arrow marks the hot zone offset into the cold zone after September 2021

F). T_{15} for the hot zone were up to 20 °C higher than the cold zone, with hot spots at 80–90 °C. These hotspots were highly localized, but spatially and temporarily variable. However, in September 2021, the hotspot expanded to include the entire hot segment of the line, along which temperatures were > 80 °C (Fig. 3). At the same time the hot–cold transition moved 5 m into the cold zone, with temperatures at the 20 m mark increasing from 25 °C in January 2020 to 90 °C in September 2021. By January 2022, the 20 m mark temperature had decreased by 40 °C, as had the extent of the hotspot. However, T_{15} levels remained higher than before June 2021 (Fig. 3). This implies an expansion of the hot zone, as well as enhanced heating of the hot zone from June 2021 onwards, before stabilization at a new level associated with unrest.

In March 2021, T_{15} for Grid1 was between 30 and 40 °C with a hotspot at 60 °C in the SE corner and a second at 46 °C in the NE corner (Fig. 4a). In June 2021, hotspots were located in the same two locations, but the SE hotspot had increased in temperature and the whole area had heated by 20 °C (Fig. 4b). By this time, temperatures at the hotspots had reached boiling point temperatures. In September 2021, almost the whole area was at boiling point (Fig. 4c). By January 2022, boiling point temperatures had focused on a NE-SW hot fissure along which temperatures were 50–60 °C (Fig. 4d). This zone was already apparent in the September grid (Fig. 4c) and persisted through May 2022 (Fig. 4e). The linear feature likely represents a line of preferential fluid circulation, such as a buried fracture. This NE-SW alignment is the direction of the rim rifts and all regional structures as controlled by the extensional stress field associated with the Tindari-Letojanni fault system (Ventura 1994; Mazzuoli et al. 1995). Temperature distributions across the FA_grid (Additional file 1: Appendix C, surface = 5500 m^2) showed similar behavior between March and June 2021.

Soil CO_2 flux was also measured along Profiles 1–4 and Grid1 (Fig. 1C). An increase in temperature between June and September 2021 was matched by an increase in soil CO_2 flux at all sites. At Grid1, for example, the average flux increased from 900 g m^{-2} d^{-1} in June 2021 to 4522 g m^{-2} d^{-1} by September. Locations of peaks in T_{15} and soil CO_2 flux on Profile2 were correlated in June and September 2021 (Fig. 5), marking high permeability locations. However, the correlation declines where surface temperatures are closer to background, an effect of lower permeability so that soil CO_2 flux is almost zero.

Fumarole field survey

Vent temperatures show a general decline following the 1988–96 unrest, with lowest levels being recorded in March 2021 (Additional file 1: Appendix G). Thereafter there was an increase in the mean temperature which, in 14 months recovered to levels higher than in 1994. To clean possible anti-correlations (due for example to very low number of fumaroles measured, cf. Additional file 1: Appendix G) we developed a thermal index (FTI):

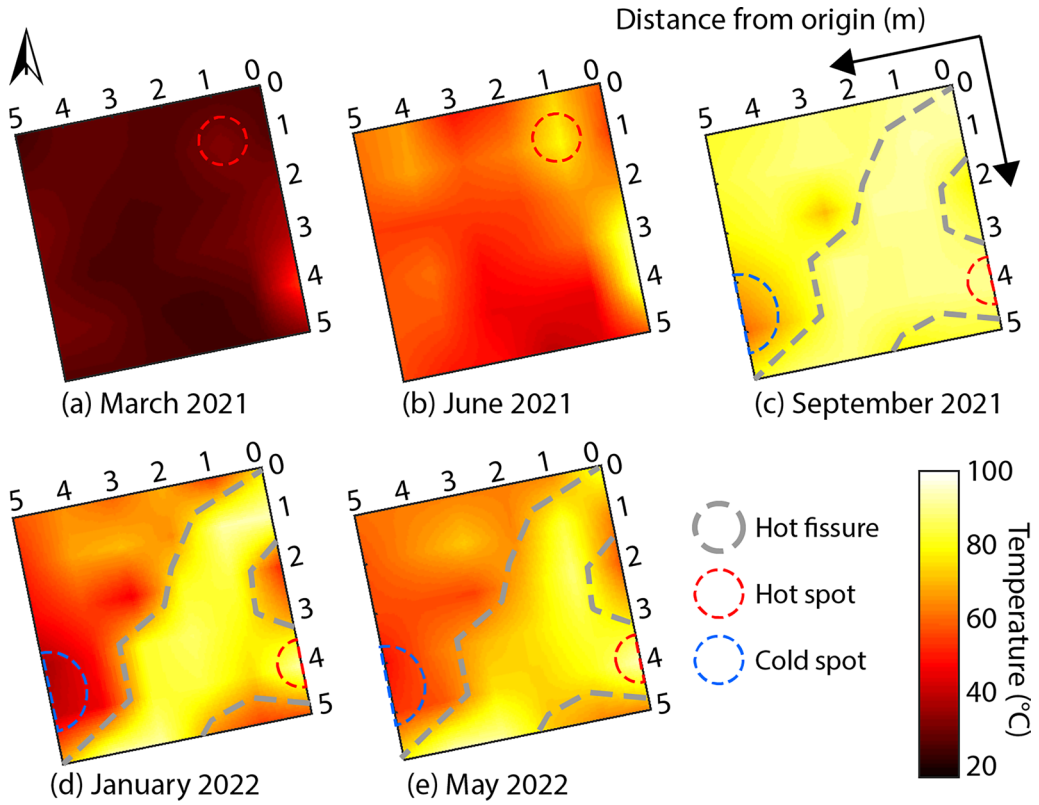

Fig. 4 T_{15} for Grid 1 (see Fig. 1C for location) in (a) March 2021, (b) June 2021, (c) September 2021, (d) January 2022 and (e) May 2022. Measurement points are interpolated with the nearest neighbor method. The hot and cold spots, either persistent or occasional, and the hot zone that runs diagonally across the area after June 2021 are indicated in the relative survey

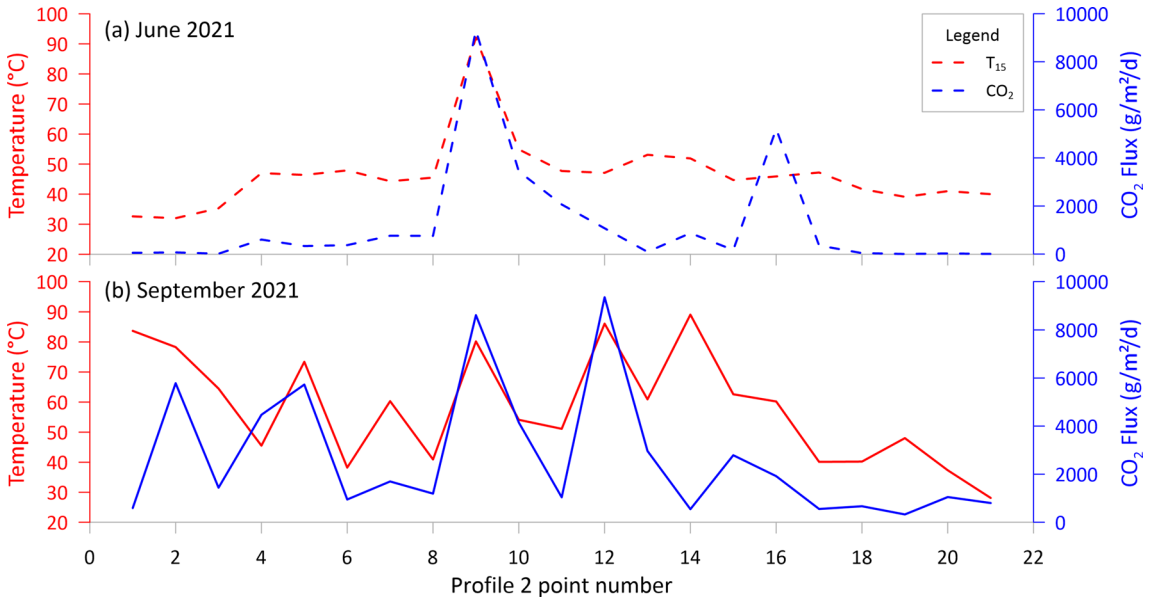

Fig. 5 Soil CO_2 flux and T_{15} on Profile2 in (**a**) June and (**b**) September 2021

$$FTI = \frac{(T_{max} * T_{mean} * Nb_v)}{SD^2 * 10^4}, \quad (5)$$

where T_{max} and T_{mean} are the maximum and mean temperatures for each survey, SD is the standard deviation and Nb_v is the number of vents measured. This index is designed to use T_{max} as a proxy for the absolute thermal state of the fumarole field, T_{mean} for the heat flux, Nb_v for the size of the fumarole field, and standard deviation for the thermal behavior, where small standard deviation has been shown to be associated with cooling, and high standard deviation with heating (Harris and Maciejewski 2000).

The FTI shows a general decline through 2021, with a recovery to around the 1996 levels by June 2022 (Fig. 6). This approach minimizes the influence of changes in permeability. Increased fracturing and fluid flow have been shown to result in increased heat flux without any change in magmatic input, as occurred between 2002 and 2010 (Gambino and Guglielmino 2008; Alparone et al. 2010; Harris et al. 2012). It thus confirms the current trend as not related to such a process. We see the same thermal reactivation from June 2021 in all zones (Additional file 1: Appendix G). Reactivation was also apparent in the field, where we observed (1) activation of a fissure network with low temperature fumaroles outside of the main fumarole field area, (2) increased sulfur deposition, (3) increased high temperature sulfur mineralization (liquid orange sulfur and black sublimates), (4) eruption of sulfur flows and sulfur pyroclasts (Additional file 1: Appendix A), and (5) melting of the sulfur component of the substrate to leave a fine-grained grey silicate powder (Harris and Maciejewski 2000).

In-situ temperature in the hot zone

We assess the magnitude of heating using the average daily surface temperature minus air temperature at GRAY_station (= ΔT). In 2020 ΔT was negligible and stable (ΔT ± 1 °C, Fig. 7). However, ΔT increased to 2–3 °C in April 2021, reaching 8 °C by the end of 2021 (Fig. 7) as the system went into unrest.

At depth of 15 cm, rainfall causes perturbations of ground temperature, where T_{15} decreased by up to 20 °C during rainfall events, and taking one day to two weeks to recover (Fig. 8). However, around these events, there was a systematic increase in T_{15} by 0.167 °C per day until August 23 at MZ1, at which point the rate increased to 0.7 °C per day through mid-September. Thereafter we record three pulses during which T_{15} reached boiling temperature. The three pulses had durations of around half a month and were centered on late-September, late-October and late-November, the later pulses marked by discrete peaks with T_{15} up to 110 °C. The time series collected at GRAY_station and, to a lesser extent, DDS mimic the behavior of MZ1, but with lower T_{15} and less marked pulses and peaks (Fig. 8). This is consistent with DDS being further from the fumarole field, where the lower temperature and response at DDS suggests lower permeability conditions than at MZ1.

Thermal camera images

Thermal images were collected on 25 June and 29 September 2021 (Fig. 9a, b) during nighttime satellite overpasses. These images showed expansion of the thermal anomaly, especially in the west and south-west sectors of the crater, where the anomaly spread into previously cold zones. It also shows reactivation of areas within the

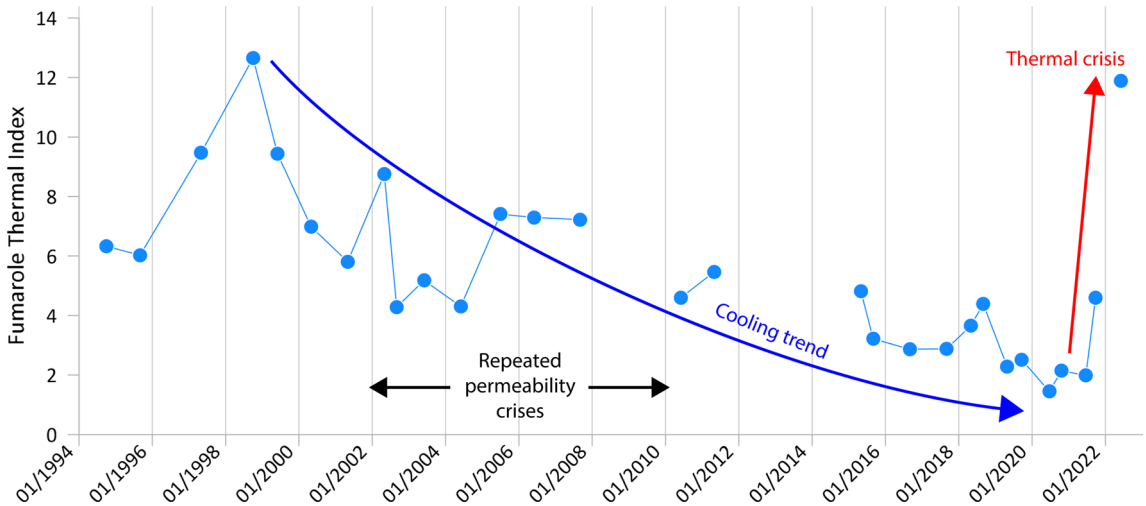

Fig. 6 Long term thermal trend of the Fossa fumarole vents. Gaps are when the period of time between two surveys is greater than 1 year. The point for January 2022 was likely underestimated due to poor visibility (plume condensation)

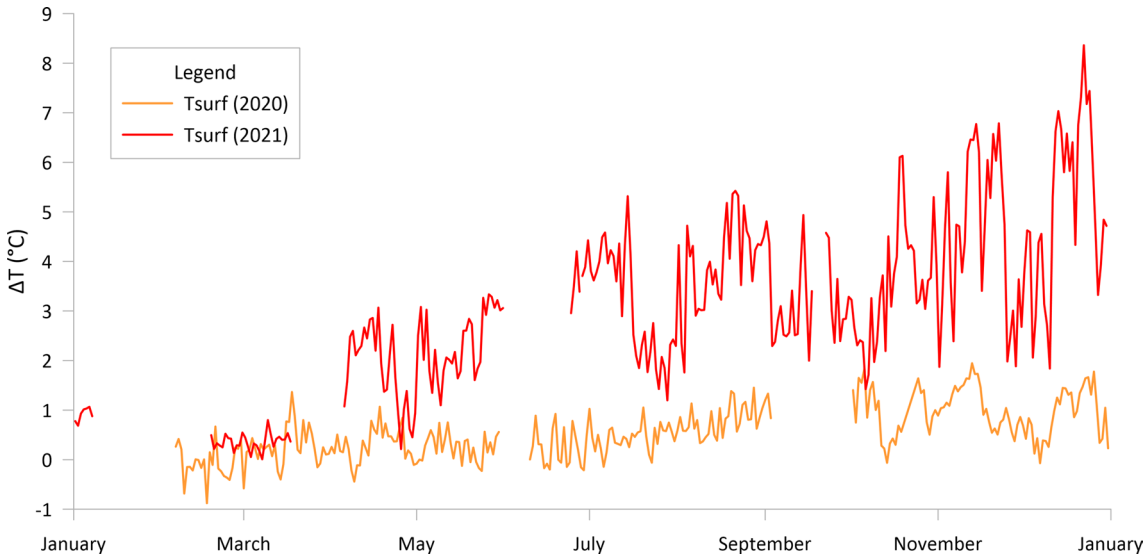

Fig. 7 Surface temperature minus air temperature at GRAY station for 2020 and 2021

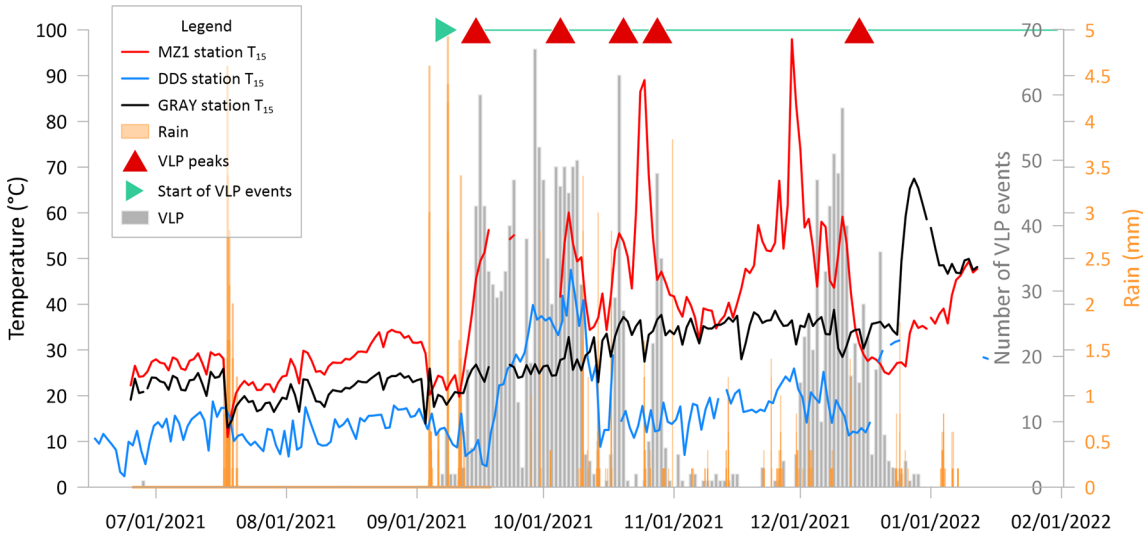

Fig. 8 T_{15}, VLP events and rainfall at MZ1, GRAY and DDS stations. VLP events are taken from Fig. 13b of Federico et al. (2023). The red triangles indicate VLP event peaks and the green line shows the onset and continuation of seismic activity registered during the unrest. Many temperatures' peaks appear synchronous with the peaks in the VLP swarms

fumarole field, especially along the rim rifts, in the upper zone and areas of the middle zone.

Surface temperature distributions are corrected for air temperature to take into account seasonal cycles, meaning that the first bins of the temperature distributions are collocated (Fig. 9c, d). The skewness in June is higher because background temperatures dominate more than in September (Fig. 9c; Table 1). September's distribution also has a more robust high temperature tail, resulting in a lower skewness and highly positive kurtosis (Table 1), indicative of heating (Harris et al. 2009). The September distribution can be separated into three populations: (1) background temperatures (normal distribution), (2) heated ground (normal distribution), and (3) pixels containing fumaroles and subsequent heated ground (skewed distribution) (Fig. 9d).

ASTER images

There was no correlation between the temporal variation of mean or maximum pixel temperatures and the

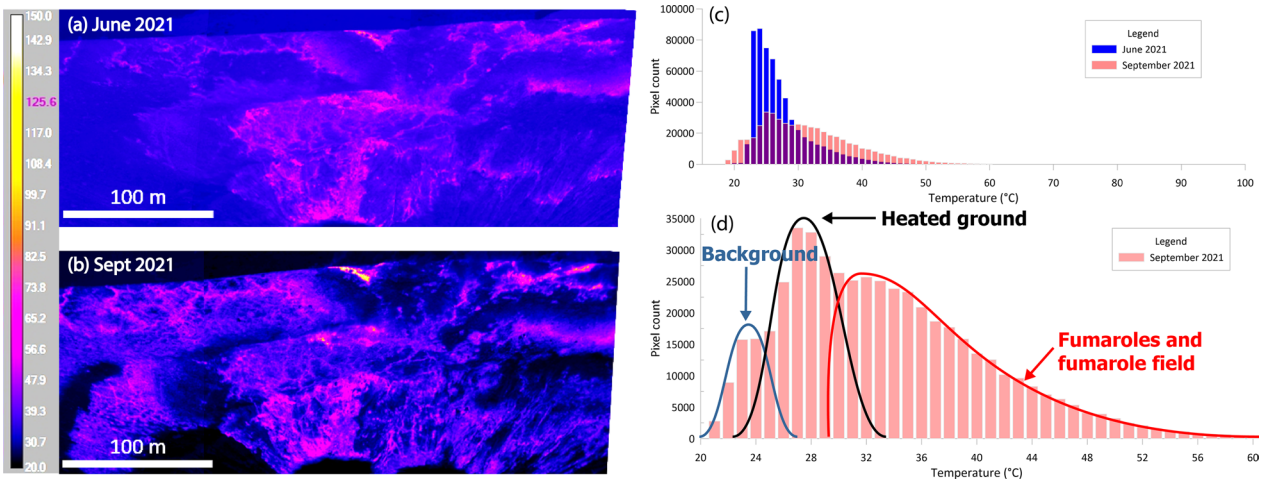

Fig. 9 Expansion of the thermal anomaly associated with the fumarole field between (**a**) June and (**b**) September 2021. The rim zone is not visible from this viewpoint. **c** Comparison of surface temperature frequency distributions from thermal camera images obtained in June and September 2021. **d** Surface temperature frequency distribution in September 2021

Table 1 Temperature statistics for the camera thermal images

	Maximum	STD	Skewness	Kurtosis
June 2021	116	4.7	2.0	7.2
Sept 2021	150	7.3	1.9	11.9

number of anomalous pixels (Additional file 1: Appendix H). However, there was plainly an increase in the size and magnitude of the anomaly (Additional file 1: Appendix D, E). We thus developed a method to highlight the thermal anomaly and extract any temporal trends using the number of anomalous pixels to take into account changes in size of the anomaly (Fig. 10). The resulting Satellite Thermal Index (STI) is given by:

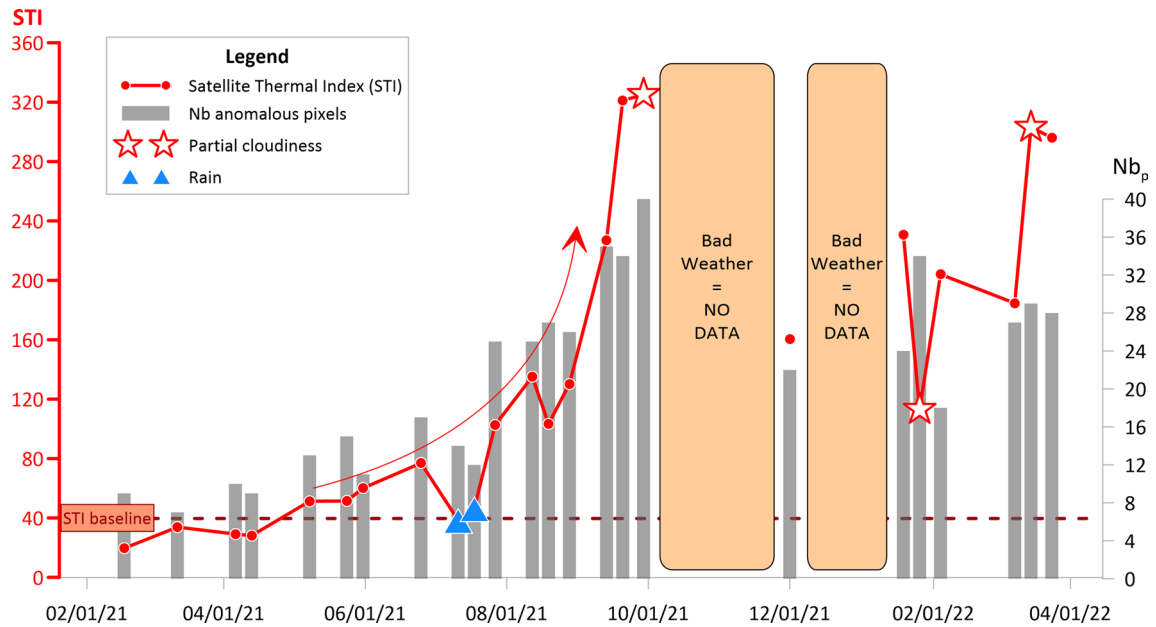

Fig. 10 ASTER-derived STI. Three scenes (09/29/21, 01/26/22 and 03/14/22) were still selected even though the cloud cover was partially covering the crater (colored star mark). The July 2021 storm events are marked by a blue triangle. The STI and NBp baselines are respectively placed at 40 and 10 pixels

$$STI = \frac{Tmax_{crater} * Tmean_{crater} * SD_{crater} * Nb_p}{Tmax_{control} * Tmean_{control} * SD_{control}}, \quad (6)$$

where $Tmean_{crater}$ is the average temperature from the anomaly, $Tmean_{control}$ is the average temperature of the ambient control area on Vulcanello, SD_{crater} is the standard deviation for the anomalous temperature distribution, $SD_{control}$ is the standard deviation on Vulcanello and Nb_p is the number of anomalous pixels. The role of the numerator is similar to that of Eq. (5) and minimizes the influence of seasonal and diurnal cycles. The index values are underestimated in case of partial cloud cover or rain fall (such as the mid-July 2021 storm event) (Fig. 10), but we see an increase possibly beginning in mid-May, to reach a first peak at the end of September 2021 (which might be underestimated because of the partial cloudiness). This is consistent with the increased number of anomalous pixels from mid-May. From September onwards the STI remained at a high level (Fig. 15). Note that trends in STI (Fig. 10) mimics those in the in-situ temperature data, providing ground truth validation.

Cross validation of heat fluxes from ASTER and VIIRS

ASTER-derived radiative heat fluxes are 4–8 MW until July 2021, increasing to 8–20 MW thereafter (Fig. 11a). The VIIRS-derived radiative heat fluxes are more scattered due to the greater pixel size (375 m) and subpixel cloud contamination, but are generally within range of ASTER-derived fluxes (Fig. 11a).

Thermal camera only targets the fumarole field on the NE inner flank, whereas ASTER and VIIRS target the cone-wide heat flux (the entire crater and all flanks). Thermal camera derived radiative heat fluxes are thus lower, being 1–2 MW (Fig. 11a), and are consistent with the VIIRS-derived radiative heat flux obtained for the same portion of the system by Coppola et al. (2022), i.e., 1.2 MW. This means that, in terms of radiative heat flux, the fumarole field contributes to 5–10% of the cone-wide flux, which is consistent with Mannini et al. (2019).

In terms of total heat flux, ASTER recorded 30–60 MW until October 2021, with a possible ramp up beginning in June. Total heat flux then increased abruptly to 80–90 MW during October 2021, with a peak at 120 MW in March 2022 (Fig. 11b). These values are higher than the flux of 21 MW calculated on the basis of steam flux in 1998 by Chiodini et al. (2005), which was at the end of the previous unrest. These total heat fluxes are also higher than the pre-unrest (2000–2015) baseline of 5–14 MW as given by Mannini et al. (2019) and as obtained from the same data (ASTER) using the same approach as applied here. The change from baseline fluxes is a result of the both the size (number of pixels) and magnitude (temperature) of the an anomaly increasing (Additional file 1: Appendix D, E).

Total heat fluxes from thermal imagery are 18 and 32 MW (Fig. 11b), being higher in September than July. This is consistent with the heating trend, and shows that the percentage contribution of the NE inner flank to the total heat flux decreased between the two acquisitions (Fig. 11b), consistent with spreading of heated zones and soil degassing chimneys onto the outer flanks.

Discussion

Gas and heat flux partitioning

There is no correlation between T_{15} and soil CO_2 flux if we consider the entire data set. One possible explanation for lack of correlation is that it is hard to seal a high-volume accumulation chamber on a rough and hard ground surface, so CO_2 can escape around the edges of the chamber. However, the primary cause is the case-hardened crust (cf. Malin et al. 1983), a 10 cm thick cemented surface layer of ash and blocks produced by alteration of hydrothermal salts. Very low permeability of this crust hinders CO_2 escape, and causes gas to flow laterally to cracks in the surface. At the same time the hardened crust will have a higher thermal conductivity than a granular material and is more efficient at transferring heat to the surface (see Tables in Clark 1966). Hot spots have a better correlation with peaks in soil CO_2 flux because they are at permeable, non-crusted locations, although we find dislocation between heat and CO_2 emission points at a meter scale (Fig. 5). This is especially true for measurements made within one meter of each other, as for example at Grid 1, where data are scattered and uncorrelated (Fig. 12b). Instead, measurements separated by several meters are beyond the spatial scale of the dislocation, improving correlation (Fig. 12a). The correlation is also better for Profile 1 in September ($R2 = 0.80$) than in June ($R2 = 0.73$) (Fig. 12a) because the number of hot spots increased (Fig. 5).

Soil temperature pulses

Three hypotheses have been used to explain the link between increased seismicity and fumarole temperatures: (1) an external cause, such as rainfall (Nakano and Kumagai 2005), (2) a transient permeability increase leading more efficient heat flux (Harris et al. 2012), and/or (3) increased release of hot gases from the deep magma body (Alparone et al. 2010; Cannata et al. 2012). We see all three effects in our data.

The temperature pulses of late-September and late-October 2021 are synchronous with the first two Very Long Period (VLP) swarms, and the VLP swarm of mid-December is followed by a temperature peak at GRAY_ station (Fig. 8). VLP events registered at Vulcano's

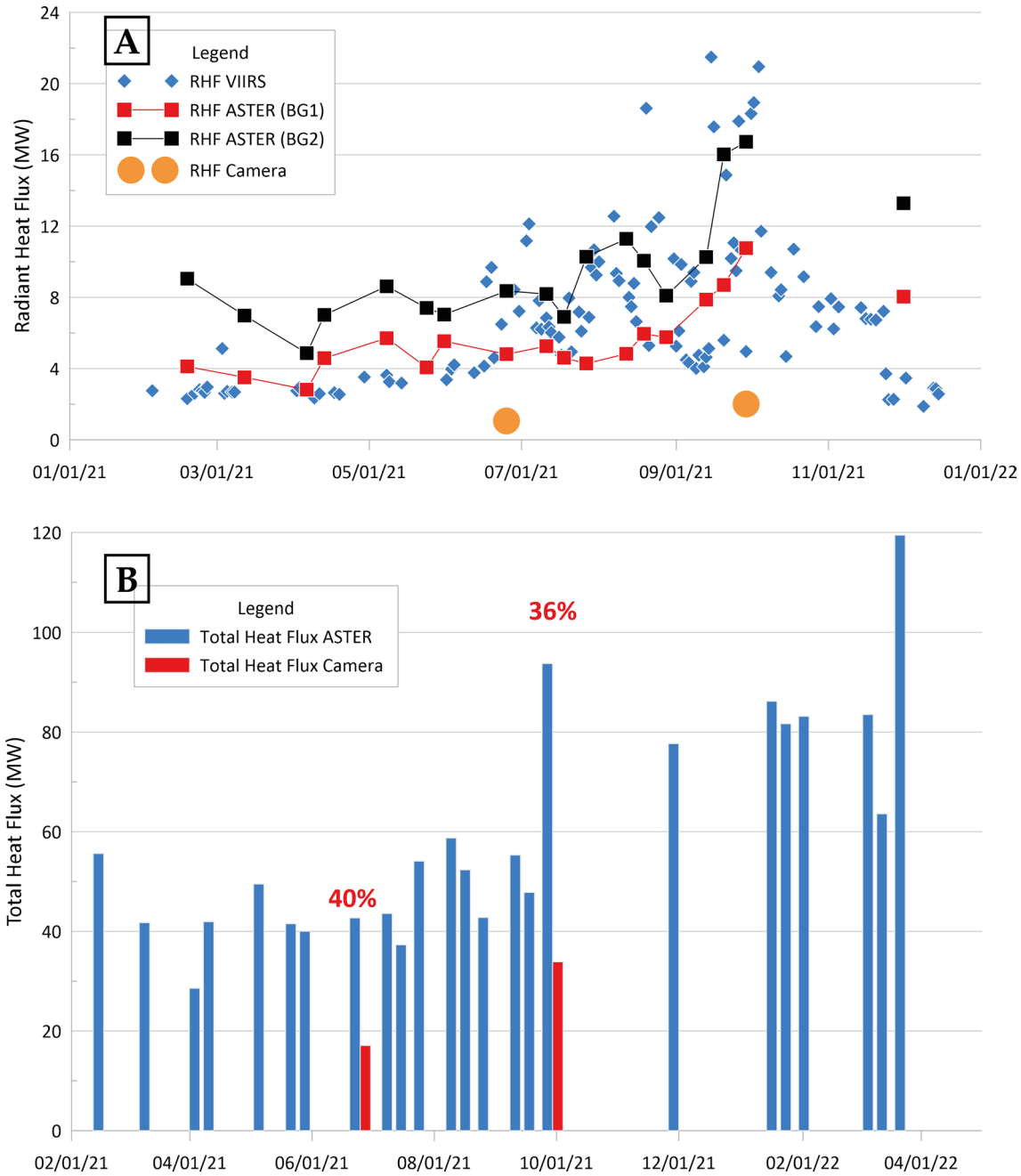

Fig. 11 **a** Comparison of Radiative Heat Flux (RHF) from ASTER, VIIRS and ground-based thermal imagery. Minimum bound for ASTER heat flux is using the first mode of temperature distribution for pixels in the Fossa ROI as background temperature (BG1). Maximum bound uses the minimum temperature from the same ROI (BG2). **b** Total heat flux time series as calculated from ASTER on the whole exposed anomaly and compared to the heat flux from ground-based thermal imagery (targeting only the inner flank of the northern slope)

hydrothermal system have been interpretated as linked to increases in the gas volume fraction in the fluid, sudden release of pressured gas, and generation of small cracks (Alparone et al. 2010; Cannata et al. 2012). In such case, fluid pressure increases to exceed the mechanical resistance of any obstruction inside hydrothermal fluid-filled cracks (=increased fracturing). The fluid flow then resonates inside the newly opened cracks (=increase of fluid flow) (Alparone et al. 2010).

Rainfall events have also been shown to trigger both VLPs and temperature changes (Nakano and Kumagai 2005), but rainfall events in our data are not

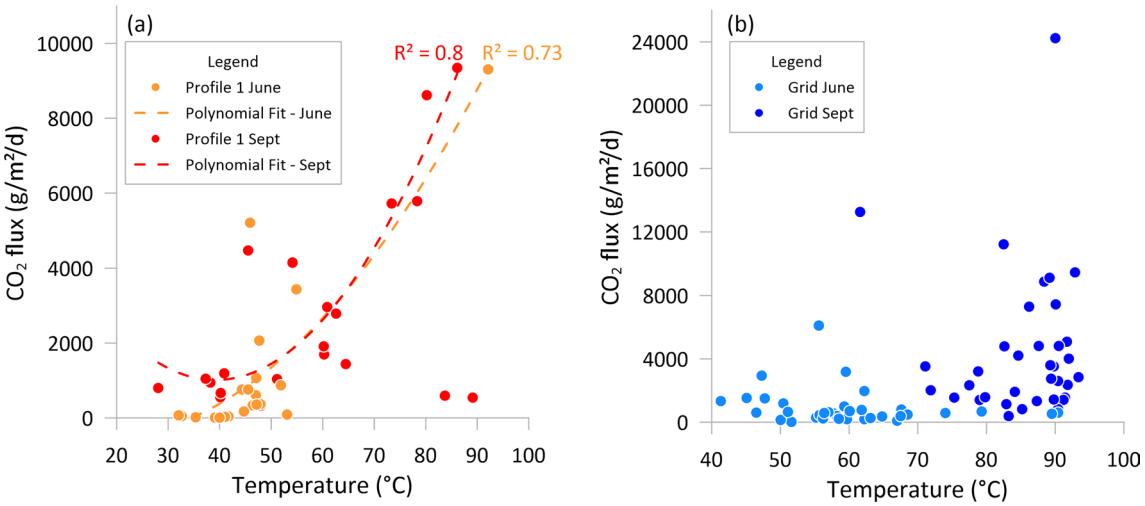

Fig. 12 **a** Comparison of T_{15} and soil CO_2 flux along Profile 1 and (**b**) across Grid 1

systematically related to VLP swarms (Fig. 8). Intense rainfall in July was not associated with any VLP events, but caused T_{15} to decrease before recovering to the level recorded before the rain event. Instead, the first VLP events of September occurred a few days after the first rain since July. This could be interpreted as a water influx which destabilized a fully-charged (inflated) and highly unstable system, which was not the case in July when the system was still charging and inflating. Discharge (out flow) then followed in October and December 2021 with the release of predominantly magma-derived fluids (Aiuppa et al. 2022) and elevated levels of seismicity and temperature (Fig. 8).

The depth of the VLP events, and thus the hydrothermal system (cf. Alparone et al. 2010; Cannata et al. 2012), at Vulcano has been estimated to be between 0.5–1.1 km b.s.l. by Alparone et al. (2010) and 0.6–1.2 km b.s.l. by Gangemi et al. (2022) in September–October 2021. The synchronicity between the VLP swarms and peaks in T_{15} at the periphery of the fumarole field (Fig. 8) suggests that fluids released from depth contributed to near-immediate surface heating. In addition, the high permeability extended over a greater area so that the heat flux became widely distributed, rather than being focused at primary fractures feeding high temperature fumaroles.

In December, fumarole temperatures plateaued at a maximum of 360 °C (Federico et al. 2023, Additional file 1: Appendix I), implying channelization towards the primary fractures. At the same time, the surface temperature response to the VLP swarm was only recorded at GRAY_station, and lagged by roughly two weeks. We interpret this as being due to less efficient heat transfer to the surface due to decreased permeability conditions. This would result from self-sealing and clogging pore space, which can occur in a relatively short timescale at a hydrothermal system (Stix and de Moor 2018; Montanaro et al. 2022; Ardid et al. 2022). By December, sealing had thus already begun at the system periphery, with sealing and channelization thus developing over the timescale of a 4 ± 2 weeks (Fig. 8).

Time-line of unrest

A summary time-line of the evolution of all data sets as the system went into unrest is given in Fig. 13. Onset of unrest is clear in all data sets, but the point in time at which unrest becomes evident is variable. In hindsight, precursors to the unrest were found at HTF, where temperatures began to increase as early as February 2021 (T3, Additional file 1: Appendix I). Increases were detected at GRAY_station during April, and in the Satellite Thermal Index in late-May, and at the fumarole on the crater rim (T2, Additional file 1: Appendix I) in June 2021. During the summer, increases in temperature were also recorded in the diffuse degassing zones (DDZ), by the FTI, at the T_{15} line and Grid 1. However, the sampling rate at these locations (every 3–4 months) limits temporal precision as to the exact month of the onset. What we do see, though, is a building thermal onset to the unrest as the system charged.

An increasing trend in soil CO_2 flux began in mid-2020. However, baseline levels were not exceeded until mid-June 2021 (Inguaggiato et al. 2022b). SO_2 flux began increasing in April 2021, exceeding the baseline sporadically in June, and persistently from August 2021 (Inguaggiato et al. 2022b). VLP events increased from zero to several hundred events per day during September (Gangemi et al. 2022), at which time CO_2 metrics also picked up (Inguaggiato et al. 2022b). During the

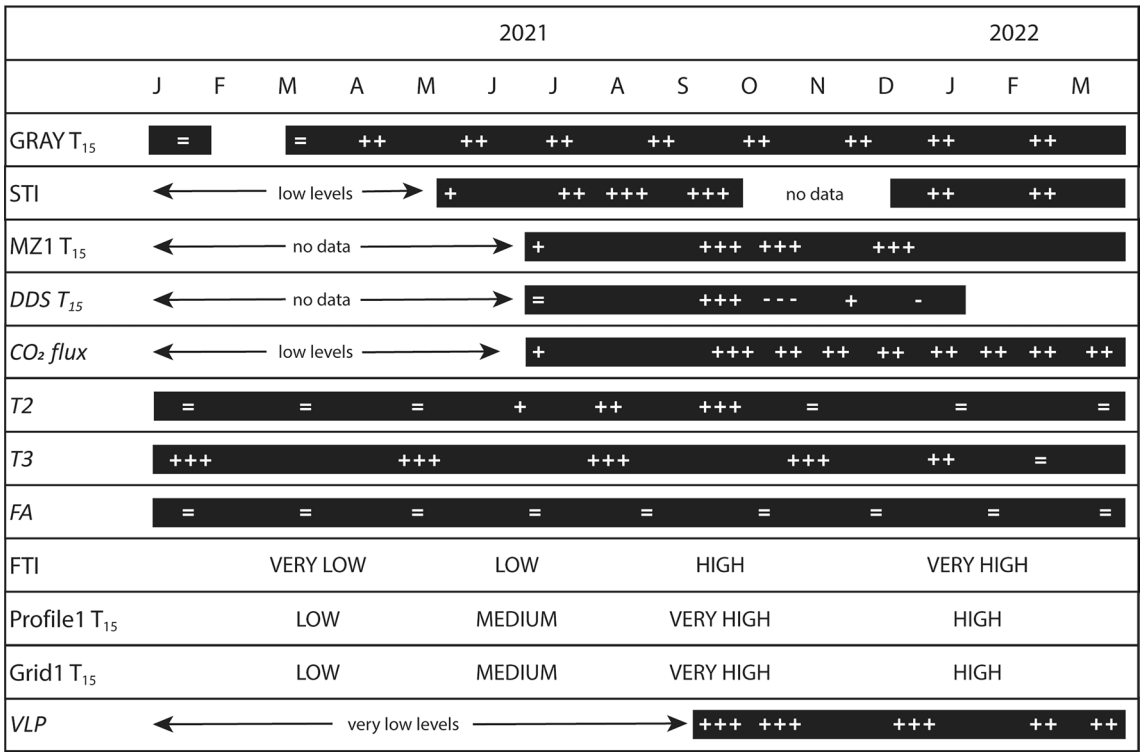

Fig. 13 Summary of unrest onset and behavior depending on the data set. CO_2 flux from the ground continuous data and repeated surveys (Inguaggiato et al. 2022a, b) and VLP events courtesy of INGV (weekly bulletins). Data in italics are from the INGV monitoring network. *FTI* Fumarole Thermal Index, *HF* Heat Flux, *IR* Infrared, *STI* Satellite Thermal Index. T2, T3 and FA are monitored HTF. The number of (+) signs gives the magnitude of the increase compared with background levels. The sign (=) means that the signal is stationary. Black rectangles indicate continuous data acquisition as opposed to punctual field campaign data

seismic crisis of mid-September, T_{15} at MZ1 increased by 40 °C in 5 days, after which T_{15} remained at, or close to, boiling point through December (Fig. 8). Our punctual mapping and profiles, showed that the presence of this boiling zone at a depth of just 15 cm was widespread (Figs. 3, 4). The geochemistry of the gas sampled from fumaroles indicates an increasingly dominant magmatic signature from July 21 onwards (Aiuppa et al. 2022; Inguaggiato et al. 2022b).

We interpret the seismic events of early September as being the failure of sealed zones. This immediately reduced the permeability of the rock above a charged system. This allowed more efficient heat and fluid flow towards the surface, explaining the equally sudden and rapid increases in soil temperature and CO_2 fluxes. Given that emissions expanded to as far as our summit sensor (SUMMIT, Fig. 1), the failure of the seal was widespread in this case extending the zone of soil discharge at-least 330 m to the south, with the ASTER hot spot expanding to encompass a large part of the cone (Additional file 1: Appendix E).

Vulcano Fossa Unrest Index

We used seven metrics, including two thermal data sets from this study and five from the monitoring network, to create a normalized Vulcano Fossa Unrest Index (VFUI):

$$VFUI = \frac{N\left[\frac{(\overline{m_{T2}}+\overline{m_{T3}}+\overline{m_{GRAY}})*\overline{m_{STI}}}{\overline{y_{RED}}}\right] + N\left[\frac{\overline{m_{CO_2}}*\overline{m_{SO_2}}}{\overline{y_{CO_2}}*\overline{y_{SO_2}}}\right] + N[\overline{m_{VLP}}]}{3}. \quad (7)$$

Here, N means that the measurement grouping has been normalized to between zero and one, where the three groupings respectively distinguish between thermal, geochemical and seismic metrics. Here, $\overline{m_x}$ is the monthly average value of parameter n and $\overline{y_x}$ is the yearly average value of parameter x. We use the monthly averaged values for T2 and T3 (Additional file 1: Appendix I), the monthly averaged difference between surface and air temperatures at GRAY_station, and monthly averaged values of STI. We combine this with monthly averaged values of soil CO_2 and SO_2 flux given

Table 2 Parameters used to calculate VFUI

	T3 (°C)	T2 (°C)	Soil CO_2 flux (g m^{-2} d^{-1})	SO_2 flux (t d^{-1})	VLP	STI	GRAY (°C)	VFUI
Jan-21	171	256	891	21	13	*20*	0.9	0.008
Feb-21	175	250	953	21	10	20	0.3	0.008
Mar-21	204	262	2009	20	7	34	0.4	0.031
Apr-21	203	267	1222	20	6	29	1.8	0.014
May-21	223	264	932	20	4	54	2.3	0.025
Jun-21	247	265	973	31	2	77	3.5	0.073
Jul-21	277	272	3148	26	0	63	3.1	0.089
Aug-21	300	281	4618	34	0	123	3.9	0.184
Sep-21	331	294	12,115	63	625	291	3.2	0.760
Oct-21	361	322	15,553	107	695	*300*	3.5	1.000
Nov-21	366	351	14,124	100	36	*200*	4.6	0.640
Dec-21	373	361	10,024	101	608	161	5.1	0.747

Parameters from left to right: monthly average temperature of fumaroles T2 and T3 (Appendix I), monthly average soil CO_2 flux and SO_2 flux (Inguaggiato et al. 2022b), monthly sum of VLP events (Instituto Nazionale Di Geofisica e Vulcanologia, 2021b, 2021a), STI and monthly average of surface temperature minus air temperature at GRAY station. The parameters generated in the course of this study are bold. STI's value in italics are estimates to fill in the gaps in ASTER images

by Inguaggiato et al. (2022b) and the monthly sum of VLP events from Federico et al. (2023). Values used are given in Table 2. The denominator for each grouping are the baseline from years of relative quiescence so as to ensure that each grouping is both weighted and unitless. Here, $\overline{y_{RED}}$ is the average surface temperature at RED_station during 2020 (4.5 °C), i.e., year of baseline data, and $\overline{y_{CO_2}}$ and $\overline{y_{SO_2}}$ are the average soil CO_2 and SO_2 fluxes over 2016–2021 as taken from Inguaggiato et al. (2022b). These were respectively 1753 g m^{-2} d^{-1} and 29 t d^{-1}. The sum of the three normalized groupings is then divided by three so that the final value for the VFUI is on a scale between zero and one.

Potter et al. (2015) developed a Volcanic Unrest Index (VUI) to communicate level of unrest to civil protection and the public, by rating unrest intensity. The approach of Potter et al. (2015) is a semi-quantitative index which uses a greater range of data types than those available here to set an unrest level between 0 and 4. Our index is likewise a semi-quantitative measure of unrest, but which uses those metrics that are available to the case in hand to detect onset of unrest, rather than assign a intensity level to ongoing unrest. In this regard the two approaches are complimentary. Although initialized with three data types (thermal, geochemical and seismic) for Vulcano, our index is designed for potential use at any hydrothermal system entering unrest and where similar monitoring data sets are available.

Our VFUI is plotted in Fig. 14 to track and categorize unrest phases based using monitoring data. The VFUI reveals four phases (Fig. 14): (1) background levels with VFUI < 5, before May 2021, (2) a precursory period through mid-August, when VFUI systematically increased to 20, (3) the onset between mid-August and mid-October, when the VFUI increased to a peak of 80, before (4) declining but remaining at elevated levels (> 50).

Thermal crisis as a sign of unrest: a model

Based on the sequence of thermal events, we can develop a four-step model for the precursory to, and onset of, unrest. While Fig. 15a describes the state of the system before unrest, Fig. 15b–d link the evolution of the thermal crisis to the phases of unrest.

1. The initial state of the system, as given in Fig. 15a, is based on the model of Nuccio et al. (1999), with a scale added for components of the system following Harris and Maciejewski (2000), Gambino and Guglielmino (2008) and Aiuppa et al. (2022). It depicts the situation described in our geological setting section whereby magmatic fluids ascend from a body at around 4 km depth into a mixing zone at 0.5–1 km b.s.l. Above the mixing zone, heat is channelized to the surface through a "chimney" (Harris and Maciejewski 2000), which is a highly permeable zone of fluid, heat and gas ascent surrounded by low permeability clays and self-sealing.
2. The thermal crisis was triggered by increased supply of magmatic fluids to the shallow hydrothermal system (Fig. 15b). This occurred between January and June 2021, as indicated by the change in geochemistry of fumarole gas samples (Aiuppa et al. 2022; Federico et al. 2023).
3. The increased supply of magmatic fluids caused an increase in heat flux, which was recorded at the sur-

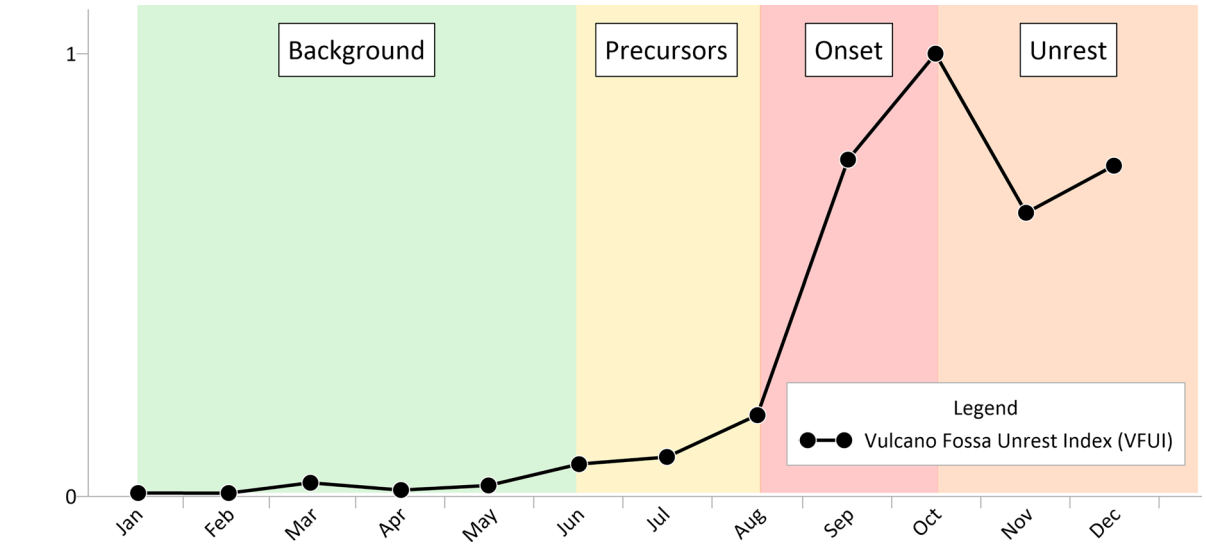

Fig. 14 Vulcano Unrest Index (VFUI) during 2021

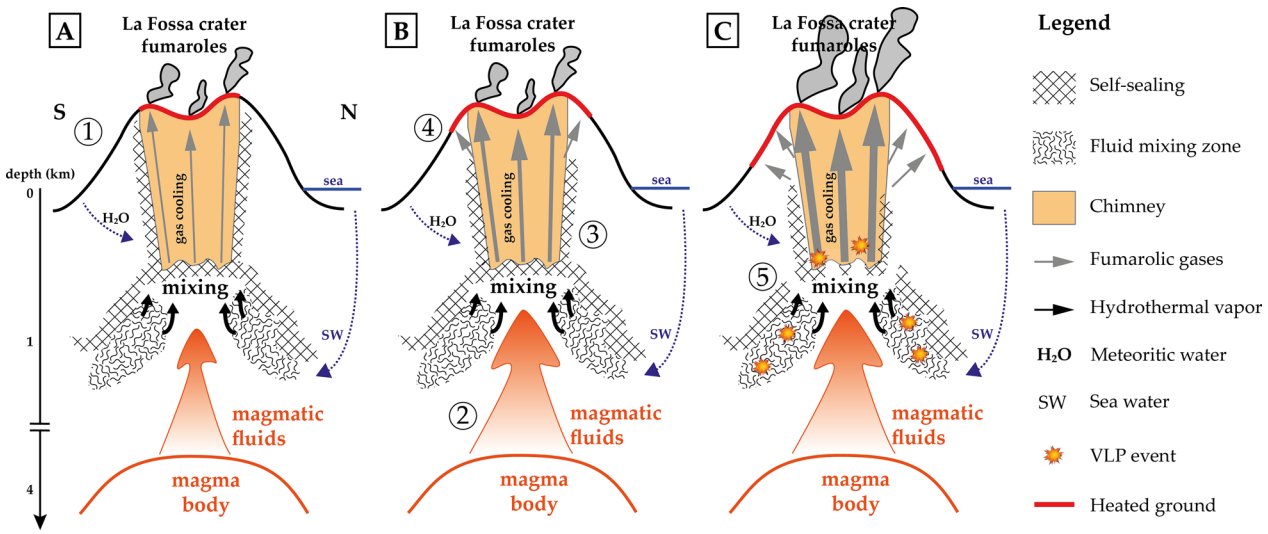

Fig. 15 Process-Response system for unrest at Vulcano during 2021. The model is designed to provide a framework to explain trends in thermal data, and is only for the hydrothermal system above the uppermost portion of the magmatic plumbing system. For detail on Vulcano's deeper plumbing system see De Astis (2013) and Alparone et al. (2010). System processes and components are based from Nuccio et al. (1999) and Harris and Maciejewski (2000). Depth for the magmatic system is from Aiuppa et al. (2022) and depth for the hydrothermal system is from (Gambino and Guglielmino 2008). Parameters in italics are taken from INGV monitoring station data and the first published papers about this unrest (Aiuppa et al. 2022; Inguaggiato et al. 2022a, b; Federico et al. 2023). Numbers 1–5 refer to the steps of the thermal evolution model during the unrest which are (1) initial state, (2) increased magma supply, (3) increased heat flux, (4) expansion of the heat chimney, and (5) seal failure. See text for detail

face beginning in February 2021 at some monitored fumaroles, and increased through June 2021 as the effect was registered at an increasing number of stations (see Figs. 13, 15b).

4. Initially, increased fluxes were focused in the heat chimney defined by self-sealing around the fractured conduit of heat and fluid ascent that had developed below the Fossa fumarole field since the end of the 1988–96 unrest (Fig. 15a), but the zone of heat emission began to spread during Spring 2021 indicating expansion of the chimney to peripheral zones of the fumarole field (Fig. 15b).

5. The impermeable seal surrounding the heat chimney failed early in September and was associated with seismic swarms, causing the area of thermal and gas emission to expand suddenly and extensively. At the same time, fluid ascent became much more efficient due to a widespread reduction in permeability so that heat and gas fluxes increased abruptly (Fig. 15c).

This 2021–2022 unrest contrasts with that of 1988–96, when expansion of the heated area was less, but during which there was activation of areas within the existing fumarole field (Bukumirovic et al. 1996, 1997). In addition, the 1988–96 unrest was characterized by a marked increase in maximum temperature (Capasso et al. 1994; Chiodini and Cioni 1995), whereas the 2021–2022 unrest was not. This suggests that the self-sealed heat chimney remained intact during the 1988–96 unrest so as to focus an increased flux in a smaller area; to be reflected in an increase in the maxima 690 °C. Instead, failure of self-sealed zones in September 2021 caused expansion of the emission zone, resulting in a widespread, but less intense, heating of the ground. Indeed, although CO_2 fluxes increased well above those of the 1988–96 unrest, maximum temperatures remained around 380 °C.

Conclusion

After two decades of relative quiescence, Vulcano entered a phase of unrest in late summer 2021 following a four to five month-long period of precursory signals. Precursory signals are mostly marked by increased heat and fluid flow to cause temperatures, gas fluxes and compositions to change. Unrest onset was then marked by an acceleration in the increase of thermal and gas emission, as well as the onset of seismicity and deformation. We show here how ground- and satellite-based thermal parameters can be used to track and characterize the phases of unrest from baseline, through precursory signs to onset. Our understanding of the 2021–2022 unrest was only possible with hindsight. However, results from this multiscale thermal approach, involving a multiparameter data comparison, will be useful for interpreting future events at Vulcano and evolving thermal conditions at less well monitored hydrothermal systems around the world.

The main difference between the current unrest and that of 1988–96 is that a much higher heat and gas flux was involved, spread over a much greater area. This was due to failure of self-sealed zones in September 2021, which did not appear to happen in the 1990s when an increased heat flux instead remained channelized in the self-sealed chimney. Aiuppa et al. (2022) explained the SO_2 degassing during October–December 2021 by the presence, at a depth of 4–5 km, of a relatively small volume ($\sim 3\times10^6$ m^3) of mafic magma. We see the charging of this injection as subtle increases in heat and gas flux, and the seal failure by an abrupt increase in these fluxes. Given the duration of previous unrest at Vulcano, this may continue for several more years. Following Selva et al. (2020), the question is: will the unrest end passively or explosively, when and how?

Abbreviations

ASTER	Advanced Spaceborne Thermal Emission and Reflection Radiometer
b.s.l.	Below sea level
DL	Datalogger
EGM	Environmental gas monitoring
FOV	Field of view
FTI	Fumarole Thermal Index
HTF	High temperature fumaroles
IR	Infrared
LOS	Line of sight
NTI	Normalized Thermal Index
RHF	Radiative heat flux
ROI	Region of interest
SD	Standard deviation
STI	Satellite Thermal Index
T_{15}	Ground temperature at 15-cm depth
TIR	Thermal infrared
VEI	Volcanic Explosivity Index
VIIRS	Visible infrared imaging radiometer suite
VLP	Very long period
VFUI	Vulcano Fossa Unrest Index

Supplementary Information

The online version contains supplementary material available at https://doi.org/10.1186/s40623-023-01913-5.

Additional file 1: **Appendix A.** Reactivation of the fumarole field – sulfur deposits and effect on vegetation. **Appendix B.** List of punctual field measurements and instruments. **Appendix C.** FA_grid. **Appendix D.** Fossa surface temperature frequency distributions from AST08. **Appendix E.** Fossa anomalous pixel detected from temperature distribution. **Appendix F.** T_{15} of the Profile1 between 2015 and 2021. **Appendix G.** Minimum and maximum and index temperatures from the fumarole surveys, by areas. **Appendix H.** Average and maximum temperatures and bimodality from the satellite survey. **Appendix I.** HTF temperatures between 2021–2023

Acknowledgements

We thank Daniel Williams (University of Pittsburgh) for completing spectral analyses of the samples to allow TIR emissivities to be set, and Massimiliano Favalli (INGV-Pisa) for making available the DEM of Vulcano Fossa as used here. Luca Teray, Roxane Buso, Stefano Mannini and Nicolas Levillayer are thanked for field help, as well as Jean Battaglia and Guillaume Georgeais for discussions regarding VLP events and application of Matlab, respectively. We would like to acknowledge Maria Grazia Di Figlia, for helping with the network's data curation and validation. We are most grateful to INGV-Palermo for making the facilities at the Carapezza Center on the island of Vulcano open and available to us. Finally, working through the Covid-19 global pandemic would not have been possible without the help and support of Tanino at the Casa Genovese (Vulcano), Maurizio at "La Forgia" (Vulcano), Manfreddi at La Giarra (Vulcano), all at the Filadelfia (Lipari), "Faraglione" bar and the Carabinieri of both Vulcano and Lipari."

Author contributions

SPB contributed to the conception and design of the project, acquisition, analysis and interpretation of the data, and wrote the original draft of the work. VF contributed to the acquisition, analysis and interpretation of the data and participated in the writing of the draft. AH contributed to the conception and

design of the project, acquisition and interpretation of the data, participated in the the original draft of the work and substantial revisions. ISD contributed to the acquisition and interpretation of the data and made substantial revisions. GG contributed to the acquisition, analysis and interpretation of the data, participated in the writing of the draft and made substantial revisions. AC contributed to the acquisition, analysis and interpretation of the data and participated in the writing of the draft. GBillota contributed to acquisition and analysis of the data with software processing. GBoudoire contributed to the acquisition, analysis and interpretation of the data and made substantial revisions. AG contributed to the acquisition and analysis of the data. FG contributed to the acquisition, analysis of the data. MR contributed to the conception of the project and made revisions.

Funding
LabEx Clervolc (program 2); ANR-DIRE (ANR-19-CE04-0014-DIRE: Prédire les crises des écosystèmes hydrothermaux volcaniques à partir de réseaux multiples de capteurs) and INGV-Palermo supported fieldwork and equipment purchase. For field missions during 2019–2022, S.P-B used a EuroVolc TransNational Access grant (EV-C2_003) for support.

Availability of data and materials
The data sets used during the current study are available from Sophie Pailot-Bonnétat on reasonable request.

Declarations

Ethics approval and consent to participate
Not applicable.

Consent for publication
Not applicable.

Competing interests
We declare no competing interests.

Author details
[1]Laboratoire Magmas et Volcans, Université Clermont Auvergne, Clermont-Ferrand, France. [2]Istituto Nazionale di Geofisica e Vulcanologia-Sessione di Palermo, Palermo, Italy. [3]Department of Geology and Environmental Sciences, University of Pittsburgh, Pittsburgh, PA, USA.

Received: 9 May 2023 Accepted: 26 September 2023
Published online: 11 October 2023

References

Aiuppa A, Bitetto M, Calabrese S et al (2022) Mafic magma feeds degassing unrest at Vulcano Island, Italy. Commun Earth Environ 3:255. https://doi.org/10.1038/s43247-022-00589-1
Alparone S, Cannata A, Gambino S et al (2010) Time-space variation of volcano-seismic events at La Fossa (Vulcano, Aeolian Islands, Italy): new insights into seismic sources in a hydrothermal system. Bull Volcanol 72:803–816. https://doi.org/10.1007/s00445-010-0367-6
Ardid A, Dempsey D, Caudron C, Cronin S (2022) Seismic precursors to the Whakaari 2019 phreatic eruption are transferable to other eruptions and volcanoes. Nat Commun 13:2002. https://doi.org/10.1038/s41467-022-29681-y
Aubert M (1999) Practical evaluation of steady heat discharge from dormant active volcanoes: case study of Vulcarolo fissure (Mount Etna, Italy). J Volcanol Geoth Res 92:412–429. https://doi.org/10.1016/S0377-0273(99)00088-8
Bukumirovic T, Italiano F, Nuccio PM et al (1996) Evolution of the fumarolic activity at La Fossa Crater of Vulcano. Acta Vulcanol 8:210–211
Bukumirovic T, Italiano F, Nuccio PM (1997) The evolution of a dynamic geological system: the support of a GIS for geochemical measurements at the fumarole field of Vulcano, Italy. J Volcanol Geoth Res 79:253–263. https://doi.org/10.1016/S0377-0273(97)00032-2
Cannata A, Diliberto IS, Alparone S et al (2012) Multiparametric approach in investigating volcano-hydrothermal systems: the case study of Vulcano (Aeolian Islands, Italy). Pure Appl Geophys 169:167–182. https://doi.org/10.1007/s00024-011-0297-z
Capasso G, Inguaggiato S, Nuccio PM et al (1994) Chemical variations in the fumarolic gases of La Fossa di Vulcano crater. Acta Vulcanol 6:41–43
Capasso G, Favara R, Inguaggiato S (1997) Chemical features and isotopic composition of gaseous manifestations on Vulcano Island, Aeolian Islands, Italy: an interpretative model of fluid circulation. Geochim Cosmochim Acta 61(16):3425–3440. https://doi.org/10.1016/S0016-7037(97)00163-4
Cappello A, Ganci G, Calvari S et al (2016) Lava flow hazard modeling during the 2014–2015 Fogo eruption, Cape Verde. J Geophys Res Solid Earth 121:2290–2303. https://doi.org/10.1002/2015JB012666
Carapezza M, Nuccio PM, Valenza M (1981) Genesis and evolution of the Fumaroles of Vulcano (Aeolian Islands, Italy): a geochemical model. Bull Volcanol 44:547–563
Chiodini G, Cioni R (1995) Origin of the fumarolic fluids of Vulcano Island, Italy and implications for volcanic surveillance. Bull Volcanol 57:99–110
Chiodini G, Cioni R, Guidi M et al (1998) Soil CO_2 flux measurements in volcanic and geothermal areas. Appl Geochem 13:543–552
Chiodini G, Granieri D, Avino R et al (2005) Carbon dioxide diffuse degassing and estimation of heat release from volcanic and hydrothermal systems. J Geophys Res Solid Earth 110:1–17. https://doi.org/10.1029/2004JB003542
Chouet BA, Matoza RS (2013) A multi-decadal view of seismic methods for detecting precursors of magma movement and eruption. J Volcanol Geoth Res 252:108–175
Christenson BW, Reyes AG, Young R et al (2010) Cyclic processes and factors leading to phreatic eruption events: Insights from the 25 September 2007 eruption through Ruapehu Crater Lake, New Zealand. J Volcanol Geoth Res 191:15–32. https://doi.org/10.1016/j.jvolgeores.2010.01.008
Clark SP (1966) Thermal conductivity. In: Clark SP (ed) Handbook of physical constants, Revised. The Geological Society of America, New York, pp 459–483
Coppola D, Laiolo M, Campus A, Massimetti F (2022) Thermal unrest of a fumarolic field tracked using VIIRS imaging bands: The case of La fossa crater (Vulcano Island, Italy). Front Earth Sci (Lausanne) 10:964372. https://doi.org/10.3389/feart.2022.964372
Corradino C, Ramsey MS, Pailot-Bonnetat S et al (2023) Detection of subtle thermal anomalies: deep learning applied to the ASTER global volcano dataset. IEEE Trans Geosci Remote Sens 61:1–15. https://doi.org/10.1109/TGRS.2023.3241085
De Fiore O (1924) Brevi note sull'attività di Vulcano (Isole Eolie) dal 1890 al 1924. Bull Volcanolog 2:7
De Astis G, Lucchi F, Dellino P et al (2013) Geology, volcanic history and petrology of vulcano (central aeolian archipelago). Geol Soc Memoir 37:281–349. https://doi.org/10.1144/M37.11
De Natale G, Troise C, Pingue F, Zollo A (1999) Earthquake dynamics during unrest episodes at Campi Flegrei Caldera (Italy): a comparison with Rabaul (New Guinea). Phy Chem Earth (a) 24:7–100
Diliberto IS (2011) Long-term variations of fumarole temperatures on Vulcano Island (Italy). Annal Geophys 54. https://doi.org/10.4401/ag-5183
Diliberto IS (2017) Long-term monitoring on a closed-conduit volcano: a 25 year long time-series of temperatures recorded at La Fossa cone (Vulcano Island, Italy), ranging from 250 °C to 520 °C. J Volcanol Geoth Res 346:151–160. https://doi.org/10.1016/j.jvolgeores.2017.03.005
Federico C, Cocina O, Gambino S et al (2023) Inferences on the 2021 ongoing volcanic unrest at Vulcano Island (Italy) through a Comprehensive Multidisciplinary Surveillance Network. Remote Sens (Basel) 15:1405. https://doi.org/10.3390/rs15051405
Ferrucci F, Gaudiosi G, Milano G, Nercessian A (1991) Seismological exploration of Vulcano (Aeolian Islands, southern Tyrrhenian sea): case history. Acta Vulcanol 1:143–152
De Fiore O (1922) Vulcano (Isole Eolie), Riv. Vulcanologica. Cozzolino, Napoli
Gambino S, Guglielmino F (2008) Ground deformation induced by geothermal processes: a model for La Fossa Crater (Vulcano Island, Italy). J Geophys Res Solid Earth 113. https://doi.org/10.1029/2007JB005016
Ganci G, Bilotta G, Cappello A et al (2016) HOTSAT: A multiplatform system for the thermal monitoring of volcanic activity using satellite data. Geol Soc Spec Publ 426:207–221. https://doi.org/10.1144/SP426.21
Ganci G, Bilotta G, Zuccarello F et al (2023) A multi-sensor satellite approach to characterize the volcanic deposits emitted during etna's lava fountaining: the 2020–2022 study case. Remote Sens (Basel) 15:916. https://doi.org/10.3390/rs15040916

Gangemi MV, Alparone S, Andrea C, et al (2022) Analysis of seismic signals accompaignying the unrest of Vulcano in 2021 [Poster Presentation] Rittmann Conference, Catania, Italy
Gaonac'h H, Vandemeulebrouck J, Stix J, Halbwachs M (1994) Thermal infrared satellite measurements of volcanic activity at Stromboli and Vulcano. J Geophys Res 99:9477–9485. https://doi.org/10.1029/93JB02392
Geshi N, Iguchi M, Shinohara H (2016) Phreatomagmatic eruptions of 2014 and 2015 in Kuchinoerabujima Volcano triggered by a shallow intrusion of magma. J Nat Dis Sci 37:67–78
Girona T, Realmuto V, Lundgren P (2021) Large-scale thermal unrest of volcanoes for years prior to eruption. Nat Geosci 14:238–241. https://doi.org/10.1038/s41561-021-00705-4
Gottsmann J, Carniel R, Coppo N, et al (2007) Oscillations in hydrothermal systems as a source of periodic unrest at caldera volcanoes: multiparameter insights from Nisyros, Greece. Geophys Res Lett 34. https://doi.org/10.1029/2007GL029594
Hamling IJ (2017) Crater lake controls on volcano stability: insights from White Island, New Zealand. Geophys Res Lett 44:11311–11319. https://doi.org/10.1002/2017GL075572
Harris A (2013) Thermal remote sensing of active volcanoes. Cambridge University Press
Harris A, Maciejewski A (2000) Thermal surveys of the Vulcano Fossa fumarole field 1994–1999: evidence for fumarole migration and sealing. J Volcanol Geotherm Res 102:119–147
Harris A, Stevenson DS (1997) Thermal observations of degassing open conduits and fumaroles at Stromboli and Vulcano using remotely sensed data. J Volcanol Geoth Res 76:175–198. https://doi.org/10.1016/S0377-0273(96)00097-2
Harris AJL, Sherman SB, Wright R (2000) Discovery of self-combusting volcanic sulfur flows. Geology 28:415–418
Harris A, Carniel R, Patrick M, Dehn J (2004) The sulfur flow fields of the Fossa di Vulcano. Bull Volcanol 66:749–759. https://doi.org/10.1007/s00445-004-0361-y
Harris A, Lodato L, Dehn J, Spampinato L (2009) Thermal characterization of the Vulcano fumarole field. Bull Volcanol 71:441–458. https://doi.org/10.1007/s00445-008-0236-8
Harris A, Alparone S, Bonforte A et al (2012) Vent temperature trends at the Vulcano Fossa fumarole field: the role of permeability. Bull Volcanol 74:1293–1311. https://doi.org/10.1007/s00445-012-0593-1
Inguaggiato S, Vita F, Diliberto IS et al (2022) The volcanic activity changes occurred in the 2021–2022 at Vulcano island (Italy), inferred by the abrupt variations of soil CO_2 output. Sci Rep 12:21166. https://doi.org/10.1038/s41598-022-25435-4
Inguaggiato S, Vita F, Diliberto IS et al (2022b) The extensive parameters as a tool to monitoring the volcanic activity: the case study of Vulcano Island (Italy). Remote Sens (Basel) 14:1283. https://doi.org/10.3390/rs14051283
Italiano F, Pecoraino G, Nuccio PM (1998) Steam output from fumaroles of an active volcano: tectonic and magmatic-hydrothermal controls on the degassing system at Vulcano (Aeolian arc). J Geophys Res Solid Earth 103:29829–29842. https://doi.org/10.1029/98jb02237
Jessop DE, Moune S, Moretti R et al (2021) A multi-decadal view of the heat and mass budget of a volcano in unrest: La Soufrière de Guadeloupe (French West Indies). Bull Volcanol 83:1–19. https://doi.org/10.1007/s00445-021-01439-2
Kato A, Terakawa T, Yamanaka Y et al (2015) Preparatory and precursory processes leading up to the 2014 phreatic eruption of Mount Ontake, Japan. Earth Planets Space 67:1–11. https://doi.org/10.1186/s40623-015-0288-x
Keller J (1980) The island of vulcano. Rend Soc Italiana Mineralog Petrolog 26:369–414
Malin MC, Dzurisin D, Sharp RP (1983) Stripping of Keanakakoi tephra on Kilauea Volcano. Hawaii Geol Soc Am Bull 94:1148. https://doi.org/10.1130/0016-7606(1983)94%3c1148:SOKTOK%3e2.0.CO;2
Mannen K, Yukutake Y, Kikugawa G et al (2018) Chronology of the 2015 eruption of Hakone volcano, Japan: geological background, mechanism of volcanic unrest and disaster mitigation measures during the crisis. Earth, Planets and Space 70:1–26. https://doi.org/10.1186/s40623-018-0844-2
Mannini S, Harris AJL, Jessop DE et al (2019) Combining ground- and ASTER-based thermal measurements to constrain fumarole field heat budgets: the case of Vulcano Fossa 2000–2019. Geophys Res Lett 46:11868–11877. https://doi.org/10.1029/2019GL084013
Matsushima N, Kazahaya K, Saito G, Shinohara H (2003) Mass and heat flux of volcanic gas discharging from the summit crater of Iwodake volcano, Satsuma-Iwojima, Japan, during 1996–1999. J Volcanol Geoth Res 126:285–301. https://doi.org/10.1016/S0377-0273(03)00152-5
Mayer K, Scheu B, Yilmaz TI et al (2017) Phreatic activity and hydrothermal alteration in the Valley of Desolation, Dominica, Lesser Antilles. Bull Volcanol 79:1–19. https://doi.org/10.1007/s00445-017-1166-0
Mazzuoli R, Tortorici L, Ventura G (1995) Oblique rifting in Salina, Lipari and Vulcano islands (Aeolian islands, southern Italy). Terra Nova 7:444–452
Mercalli G (1883) Isola Vulcano. In: Arnaldo Forni (ed) Vulcani e Fenomeni Vulcanici in Italia. Biblioteca di Sismologia, Milanno, pp 146–162
Mercalli G (1907) Vulcani attivi della terra: morfologia—dinamismo—prodotti—distribuzione geografica—cause, U. Hoepli
Mercalli G, Silvestri O (1891) L'eruzione dell'Isola di Vulcano incominciata il 3 agosto 1888 e terminata il 22 marzo 1890. Annal Dell'ufficio Centrale Meteorol Geodinam 10:71–281
Meyer B (1976) Elemental sulfur. Chem Rev 76(3):367–388
Montalto A (1994) Seismic events at Vulcano (Italy) during 1988–1992. J Volcanol Geoth Res 60:193–206
Montanaro C, Mick E, Salas-Navarro J et al (2022) Phreatic and hydrothermal eruptions: from overlooked to looking over. Bull Volcanol 84:64. https://doi.org/10.1007/s00445-022-01571-7
Moretti R, Komorowski JC, Ucciani G et al (2020) The 2018 unrest phase at La Soufrière of Guadeloupe (French West Indies) andesitic volcano: scrutiny of a failed but prodromal phreatic eruption. J Volcanol Geotherm Res 393:106769. https://doi.org/10.1016/j.jvolgeores.2020.106769
Nakano M, Kumagai H (2005) Response of a hydrothermal system to magmatic heat inferred from temporal variations in the complex frequencies of long-period events at Kusatsu-Shirane Volcano, Japan. J Volcanol Geoth Res 147:233–244. https://doi.org/10.1016/j.jvolgeores.2005.04.003
Nuccio PM, Paonita A, Sortino F (1999) Geochemical modeling of mixing between magmatic and hydrothermal gases: the case of Vulcano Island, Italy
Orsi G, Petrazzuoli SM, Wohletz K (1999) Mechanical and thermo-fluid behaviour during unrest at the Campi Flegrei caldera Italy. J Volcanol Geoth Res 91:453–470. https://doi.org/10.1016/S0377-0273(99)00051-7
Potter SH, Scott BJ, Jolly GE et al (2015) Introducing the Volcanic Unrest Index (VUI): a tool to quantify and communicate the intensity of volcanic unrest. Bull Volcanol 77:1–15. https://doi.org/10.1007/s00445-015-0957-4
Ramsey M (2016) Synergistic use of satellite thermal detection and science: a decadal perspective using ASTER. Geol Soc Special Publ 426:115–136. https://doi.org/10.1144/SP426.23
Rogic N, Cappello A, Ganci G et al (2019) Spaceborne EO and a combination of inverse and forward modelling for monitoring lava flow advance. Remote Sens (Basel) 11:3032. https://doi.org/10.3390/rs11243032
Sachpazi M, Kontoes C, Voulgaris N et al (2002) Seismological and SAR signature of unrest at Nisyros caldera, Greece. J Volcanol Geoth Res 116:19–33
Sekioka M, Yuhara K (1974) Heat flux estimation in geothermal areas based on the heat balance of the ground surface. J Geophys Res 79:2053–2058. https://doi.org/10.1029/jb079i014p02053
Selva J, Bonadonna C, Branca S, De Astis G, Gambino S, Paonita A, Pistolesi M, Ricci T, Sulpizio R, Tibaldi A, Ricciardi A (2020) Multiple hazards and paths to eruptions: a review of the volcanic system of Vulcano (Aeolian Islands, Italy). Earth Sci Rev 207:103186. https://doi.org/10.1016/j.earscirev.2020.103186
Sicardi L (1940) Il recente ciclo dell'attività fumarolica dell'isola di Vulcano. Bull Volcanolog 7:85–139. https://doi.org/10.1007/BF02994895
Silvestri M, Rabuffi F, Pisciotta A et al (2019) Analysis of thermal anomalies in volcanic areas using multiscale and multitemporal monitoring: Vulcano Island test case. Remote Sens (Basel) 11:134. https://doi.org/10.3390/rs11020134
Sorey ML, Farrar CD, Gerlach TM, et al (2000) Invisible CO_2 gas killing trees at Mammoth Mountain, California. US Geological Survey Fact Sheet 172–96
Stix J, de Moor JM (2018) Understanding and forecasting phreatic eruptions driven by magmatic degassing. Earth Planets Space 70:1–19. https://doi.org/10.1186/s40623-018-0855-z
Tedesco D, Toutain JP, Allard P, Losno R (1991) Chemical variations in fumarolic gases at Vulcano Island (Southern Italy): seasonal and volcanic effects. J Volcanol Geoth Res 45:325–334. https://doi.org/10.1016/0377-0273(91)90066-9

Tedesco D, Miele G, Sanob Y, Toutain JP (1995) Helium isotopic ratio in Vulcano island fumaroles: temporal variations in shallow level mixing and deep magmatic supply. J Volcanol Geoth Res 64:117–128. https://doi.org/10.1016/0377-0273(94)00045-I

Ventura G (1994) Tectonics, structural evolution and caldera formation on Vulcano Island (Aeolian Archipelago, southern Tyrrhenian Sea). J Volcanol Geoth Res 60:207–224

Werner C, Hurst T, Scott B, et al (2008) Variability of passive gas emissions, seismicity, and deformation during crater lake growth at White Island Volcano, New Zealand, 2002–2006. J Geophys Res Solid Earth 113. https://doi.org/10.1029/2007JB005094

Wright R, Flynn L, Garbeil H et al (2002) Automated volcanic eruption detection using MODIS. Remote Sens Environ 82:135–155. https://doi.org/10.1016/S0034-4257(02)00030-5

Zuccarello F, Bilotta G, Cappello A, Ganci G (2022) Effusion rates on Mt. Etna and their influence on lava flow hazard assessment. Remote Sens (Basel) 14:1366. https://doi.org/10.3390/rs14061366

Publisher's Note